Accepted Manuscript
Version of record at: https://doi.org/10.1109/TAES.2022.3147136

Multi-Channel Clutter Modeling, Analysis, and Suppression for Missile-borne Radar Systems

Penghui Huang, Enghui Hunag, Hao Yang, Zihao Zou, Xiang-Gen Xia, and Guisheng Liao

When a missile-borne radar system works in downward-looking surveillance mode, the broadened ground clutter signal in virtue of platform high-speed motion will be received by the radar receiver, which will cause difficulty in moving target detection and attacking. Unlike airborne and spaceborne platforms, a missile-borne platform exhibits some unique motion characteristics, such as diving, spinning, and coning, causing the clutter space-time distribution property significantly different from those of airborne and spaceborne radar platforms. In addition, the forward target striking requirements make the missile-borne clutter space-time spectrum further exhibit the severe range-dependent property. To deal with these issues, accurate motion modeling of a missile-borne radar platform is firstly carried out in this paper, where the complex platform motions including forward-looking diving, spinning, and coning are considered. Then, the autocorrelation processing combined with Iterative Adaptive Approach (IAA) is applied to estimate the clutter angle-Doppler center frequencies, so as to effectively realize the clutter non-stationary compensation along spatial and temporal directions. Finally, a time-domain sliding window based subspace projection (TSWSP) method is proposed to achieve the robust clutter suppression. Both simulation and real-measured radar data processing results are presented to validate the effectiveness and feasibility of the proposed algorithm.

This work was supported in part by the National Natural Science Foundation Program of China under Grants 62171272, and in part by the USCAST2021 and SAST2019-071.
(Corresponding author: Hao Yang).

P. H. Huang, H. Yang, and Z. H. Zou are with the School of Electronic Information and Electrical Engineering, Shanghai Jiao Tong University, Shanghai 200240, China (e-mail: huangpenghui@sjtu.edu.cn; yh130058@sjtu.edu.cn; zouzihao@sjtu.edu.cn).

X.-G. Xia is with the Department of Electrical and Computer Engineering, University of Delaware, Newark, DE 19716, USA (e-mail: xxia@ee.udel.edu).

G. S. Liao is with the National Laboratory of Radar Signal Processing, Xidian University, Xi'an 710071, China (e-mail: liaogs@xidian.edu.cn).

I. Introduction

Recently, with the rapid change of battlefield environment and the emergence of advanced military moving targets, the modern battlefield situation becomes more and more complex, causing the high-threat moving target difficult to be detected and tracked. As a strategic weapon, a missile can effectively realize the time-sensitive moving target striking and becomes more and more important in a modern war. In order to further improve the missile attacking performance, the accurate guidance technology and active guidance ability are required, which will make the new-generation guided missiles exhibit the powerful capabilities of beyond-line-of-sight launch in day or night under all-weather condition [1].

For the traditional ground-based radars, moving target indication (MTI) [2]-[5] or adaptive MTI (AMTI) [6]-[8] technique can be applied to notch the scene clutter and realize the target detection based on 1-D Doppler filtering. However, for a missile-borne platform, due to its complex motion characteristics, the clutter spectrum will be severely diffused, making the typical MTI and AMTI methods invalid. Therefore, for the Doppler-extended clutter, how to extract the high-dimensional signal features to realize the extended clutter cancellation is of great research significance. To deal with this issue, Brennan *et al*. proposed the 2-D space-time adaptive processing (STAP) [9], [10] to accomplish the adaptive clutter suppression and target spatial synthesis, remarkably improving the weak moving target detection performance. However, the calculation of the joint space-time weight vector is computationally complex, and the computational complexity grows exponentially as the system dimensionality increases [11]. In addition, the statistically independent and identically distributed (i.i.d.) training data support requirement increases drastically in order to attain the clutter rejection performance corresponding to 3dB level below the optimum processing [12]. Therefore, the dimension-reduced STAP techniques become necessity to satisfy the real-time requirement in practice.

In recent years, many good dimension-reduced STAP algorithms have been proposed, which can be mainly categorized into two kinds: fixed structure dimension-reduced STAP methods [13]-[18] and adaptive dimension-reduced STAP methods [19]-[23], also known as rank-reduced STAP methods, such as principal component method [24]-[26], cross spectral metric (CSM) method [27], and subspace projection (SP) method [28], [29]. These rank-reduced STAP methods can deal with the issue of the space-time covariance matrix estimation via the range training samples and thus may be more suitable for the heterogeneous scene [20], [21].

Although the adaptive dimension-reduced STAP methods may be suboptimal due to the loss of signal components that lie in the clutter subspace, they can obtain the robust clutter filtering performance since they are not dependent on the presumed signal form or clutter distribution, providing an acceptable solution under the relatively inhomogeneous clutter scenario. Unfortunately, for a missile-borne radar system, because of the complex platform motions, such as diving, spinning, and coning, the ground stationary scatterers will show

Accepted Manuscript
Version of record at: https://doi.org/10.1109/TAES.2022.3147136

the severe non-stationarity, which will destruct the i.i.d. nature of the observed clutter components, resulting in the severe performance deterioration by using the conventional dimension-reduced and rank-reduced STAP methods [30], [31]. Therefore, how to implement the adaptive angle- and Doppler-dependence compensation and further improve the stationary clutter filtering performance are worth of investigation.

In this paper, motion models of the observed clutter on a missile-borne radar platform are firstly established, where transmitted and received 2-D array patterns are calculated with the considerations of platform complex motions, such as diving, spinning, and coning motion. Then, the time-domain autocorrelation function is constructed to realize the Doppler center estimation corresponding to every range unit, so as to achieve the clutter Doppler center alignment. In addition, due to the limited spatial degree of freedom in a space-limited missile system, the Iterative Adaptive Approach (IAA) [32]-[35] technology combined with the global least square (GLS) [36] is employed to accomplish the spatial spectrum center estimation and compensation. Finally, after the 2-D non-stationary compensation, a novel multi-channel processing technique, named the time-domain sliding window based subspace projection (TSWSP) method, is proposed to accomplish the robust clutter suppression. Both simulation and real-measured radar data are utilized to illustrate the effectiveness and applicability of the proposed algorithm.

The remainder of this paper is organized as follows: In Section II, a 3-D motion model of a missile-borne platform with diving, spinning, and coning is established on the basis of the side-looking and forward-looking configurations, where the array pattern, and range-azimuth resolutions under different motion statements are analyzed. In addition, the echo signal model of multi-channel clutter is established. In Section III, the 2-D non-stationary clutter compensation method based on IAA, autocorrelation method, and GLS method are introduced. Thereafter, the TSWSP algorithm is proposed to accomplish the robust clutter suppression. Section IV presents some simulated and real data processing results and gives discussions and comparisons to validate the proposed algorithm. Finally, some conclusions are summarized in Section V.

II. Signal Model of Missile-Borne Radar

A. Missile-borne Radar Motion Model

In this section, three kinds of missile-borne radar motion configurations are introduced, i.e., level flight with side-looking mode, level flight with forward-looking mode, and diving flight with forward-looking mode, where the rotational motions including spinning and coning are considered, providing the foundation for the subsequent clutter modelling and suppression in a multi-channel missile-borne radar system.

1) Clutter Motion Model in a Level Flight Statement with Side-Looking Mode

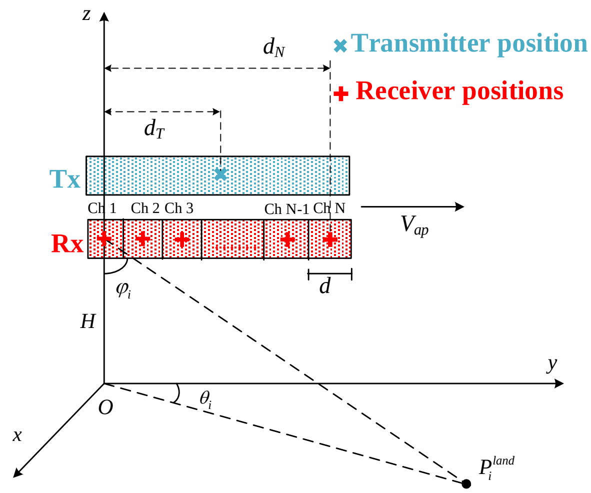

Fig. 1. 3-D geometry between the missile-borne radar platform and a ground static scatterer in a side-looking observation configuration.

The geometry configuration between a side-looking missile-borne radar system in a level flight statement and a ground scatterer, denoted by P_i^{land}, is shown in Fig.1. It is defined in a 3-D Cartesian coordinate system as *O-xyz*, with *y-axis* denoting the along-track velocity direction, *x-axis* representing the ground range coordinate, and *z*-axis determined by the right-hand rule. For this ground scatterer P_i^{land}, its equivalent self-transmitting and self-receiving instantaneous slant-range corresponding to the *n*th spatial channel can be given by

$$\begin{aligned} R_{n,i}^{land}(t_m) &= \frac{1}{2}\left[\sqrt{\begin{aligned}&(H\tan\varphi_i\sin\theta_i)^2+H^2\\ &+(H\tan\varphi_i\cos\theta_i-d_T-V_{ap}t_m)^2\end{aligned}}\right.\\ &\quad\left.+\sqrt{\begin{aligned}&(H\tan\varphi_i\sin\theta_i)^2+H^2\\ &+(H\tan\varphi_i\cos\theta_i-d_n-V_{ap}t_m)^2\end{aligned}}\right] \\ &\approx R_{0,i}-\sin\varphi_i\cos\theta_i V_{ap}t_m+\frac{(d_T+d_n)V_{ap}t_m}{2R_{0,i}} \\ &\quad-\frac{\sin\varphi_i\cos\theta_i(d_T+d_n)}{2}+\frac{V_{ap}^2t_m^2}{2R_{0,i}}+\frac{d_T^2+d_n^2}{4R_{0,i}} \end{aligned} \tag{1}$$

where $t_m = m\cdot PRT$ denotes the slow-time variable with *PRT* representing the pulse repetition time, $R_{0,i}=H/\cos\varphi_i$ denotes the initial slant-range, *H* represents the platform height, V_{ap} is the platform velocity, θ_i and φ_i denote, respectively, the azimuth angle and the elevation angle of this scatterer relative to the radar array, d_T is the distance between the transmitted channel and the reference channel (the first channel is chosen as the reference channel), $d_n=(n-1)d, n=1,2,\cdots,N$ is the distance between the *n*th received channel and the reference channel, *d* represents the physical distance between two adjacent channels, and *N* corresponds to the number of azimuth

Accepted Manuscript
Version of record at: https://doi.org/10.1109/TAES.2022.3147136

received channels. In addition, the azimuth registration error is ignored in (1) since it can be approximately compensated by using the prior radar system parameters in a low-resolution warning surveillance mode [37].

Obviously, it can be forecasted from (1) that in this ideal side-looking observation mode, the ground clutter will be represented as the linear trajectory in the space-time power spectrum plane since the clutter cone angle keeps the one-to-one correspondence relationship with the Doppler frequency, beneficial to the subsequent clutter rejection by using the spatially adaptive beamforming technique.

2) Clutter Motion Model in a Level Flight Statement with Forward-Looking Mode

When the missile-borne radar works in the forward-looking mode, the antenna panel is installed along x-axis, as depicted in Fig. 2. Then, the two-way slant-range between the ground scatterer and the nth received channel can be expressed as

$$\begin{aligned} R_{n,i}^{land}\left(t_m\right) &= \frac{1}{2}\left[\begin{array}{l}\sqrt{R_{T,x}^2\left(t_m\right)+R_{T,y}^2\left(t_m\right)+R_{T,z}^2\left(t_m\right)} \\ +\sqrt{R_{R,x}^2\left(t_m\right)+R_{R,y}^2\left(t_m\right)+R_{R,z}^2\left(t_m\right)}\end{array}\right] \\ &\approx R_{0,i}-\sin\varphi_i\cos\theta_i V_{ap}t_m+\frac{\sin\varphi_i\sin\theta_i\left(d_T+d_n\right)}{2} \\ &\quad+\frac{V_{ap}^2t_m^2}{2R_{0,i}}+\frac{d_T^2+d_n^2}{4R_{0,i}} \end{aligned} \tag{2}$$

Compared with the side-looking slant-range in (1), it is observed from (2) that for a given Doppler bin, the cone angles with respect to spatial frequencies in different range units do not coincide in the forward-looking configuration, which will make the ground clutter exhibit the severe range dependence property, destructing the i.i.d. nature of clutter samples.

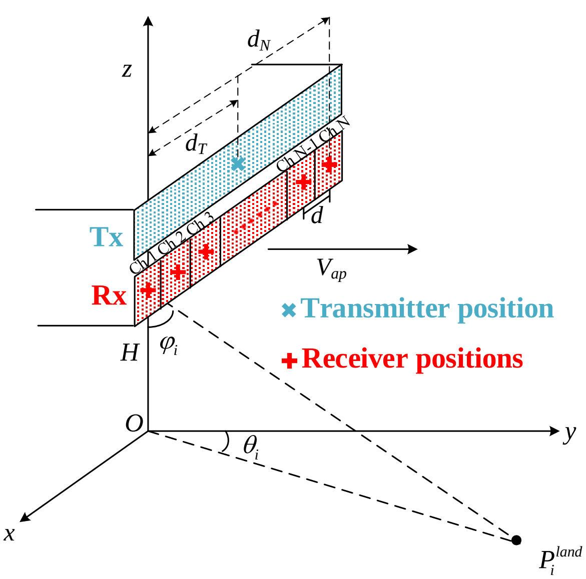

Fig. 2. 3-D geometry between the missile-borne platform and a ground static scatterer with the forward-looking level flight configuration.

3) Clutter Motion Model in a Diving Flight Statement with Forward-Looking Mode

In practice, the missile may work in a diving flight statement in order to realize the target striking [38], and then the clutter space-time coupling property will become more complex since the platform velocity direction will not be parallel with the ground surface, as displayed in Fig. 3.

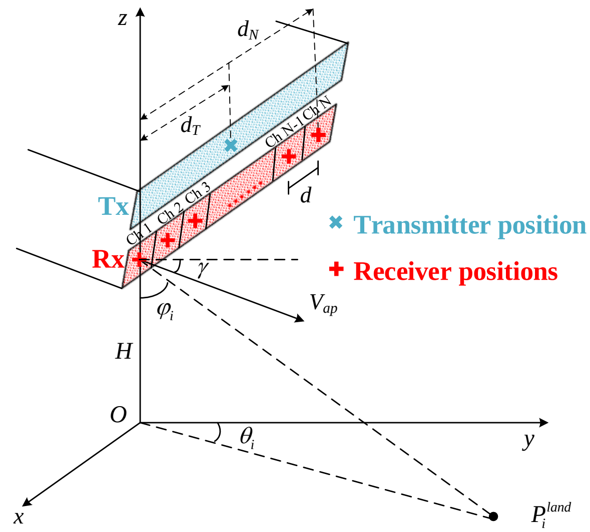

Fig. 3. 3-D geometry between the missile-borne platform and a ground static scatterer with the forward-looking diving flight mode.

From Fig. 3, it can be seen that when the diving angle, denoted by γ, is present, the slant-range history in this diving flight statement will be different from that of the level flight mode since the platform velocity component along z-axis is introduced. For the same reason, the instantaneous slant-range related to the nth received channel can be noted as

$$\begin{aligned} R_{n,i}^{land}\left(t_m\right) &\approx R_{0,i}-\left(\sin\varphi_i\cos\theta_i\cos\gamma+\cos\varphi_i\sin\gamma\right)V_{ap}t_m \\ &\quad+\frac{\sin\varphi_i\sin\theta_i\left(d_T+d_n\right)}{2}+\frac{V_{ap}^2t_m^2}{2R_{0,i}}+\frac{d_T^2+d_n^2}{4R_{0,i}} \end{aligned} \tag{3}$$

Obviously, one can see from (3) that the clutter space-time coupling is more complex due to the existence of diving angle, indicating that the clutter non-stationary phenomenon is more severe. It should be noted that when two angles γ and φ_i mutually complementary, i.e., $\gamma+\varphi_i=\frac{\pi}{2}$, the non-stationary level of ground clutter is relatively low, as demonstrated in Appendix A.

4) Clutter Motion Model in a Diving Flight Statement with Spinning and Coning Motions

In practice, the missile-borne platform may possess the complex rotation motions in order to eliminate the thrust misalignment influence and enhance the reliability for flight control system, thus increasing the guidance, control, and attack performances of the missile weapon [39]-[42]. During the missile aviation procedure with complex rotations, the Magnus effects [43] and gyroscopic effects [44] will be present, making the rotated missile exhibit the specific dynamic characteristics, i.e., the spinning and coning motions [45]-[48].

Accepted Manuscript
Version of record at: https://doi.org/10.1109/TAES.2022.3147136

Then, the above-mentioned clutter motion models in (1) ~ (3) will introduce the large model mismatch errors. To deal with this issue, a precise clutter model with the considerations of complex rotation motions is proposed in the following section.

a) 3-D Motion Model in the Case of Spinning and Coning

In addition to the diving flight, the missile body may possess the spinning and coning motions, where the nutation motion influence can be ignored when the missile platform stays in a stabilized flight statement [49], [50]. Suppose that the missile platform has a coning angle of α_0 (i.e., the antenna panel center rotates from point $O_{ap,ref}$ to point O_{ap}), and the direction of translational velocity V_{ap} is parallel to the zOy plane. For convenience, assume that *z-axis* refers to the longitudinal axis with respect to the rotated antenna panel center, which is different from the *z-axis* defined in Fig. 3. Then, *x-axis* is determined according to the right-hand rule, and thus the ground reference coordinate system *O-xyz* is built, with the 3-D motion configuration shown in Fig. 4.

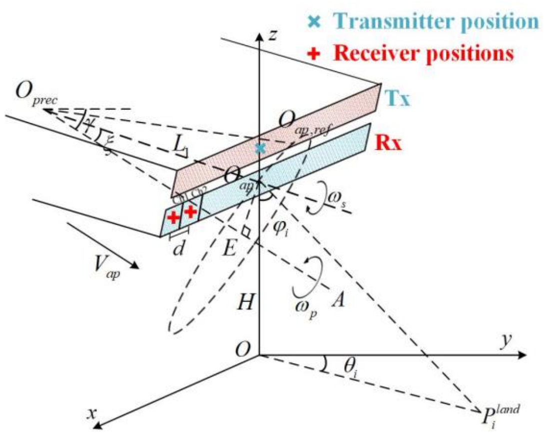

Fig. 4. 3-D geometry between the missile-borne platform and a ground static scatterer with the considerations of spinning and coning motions.

In Fig. 4, O_{prec} is the intersection point of the coning axis and missile body axis, O_{ap} is the antenna panel center point, $O_{ap,ref}$ corresponds to the antenna panel center in the highest position, E denotes the rotational center when the antenna panel undergoes the coning motion, $\overline{O_{prec}A}$ is the coning axis (also refers to the translational velocity direction), γ is the diving angle, ξ is the intersection angle between the missile body axis $\overline{O_{prec}O_{ap}}$ and the translational velocity direction $\overline{O_{prec}A}$, L_1 is the distance from the intersection point O_{prec} to the antenna panel center point O_{ap}, d denotes the physical distance between two adjacent received channels along azimuth dimension, $d_n = \frac{N-1}{2}d - (n-1)d\left(n = 1, 2, \cdots, N\right)$ denotes the physical distance between the nth channel and the reference channel (the first channel is set as the reference channel), N is the number of azimuth received channel, ω_s is the angular velocity with respect to the missile body axis, and ω_p corresponds to the angular velocity of coning motion. For an arbitrary ground scatter P_i^{land} with the azimuth angle of θ_i and the elevation angle of φ_i, in order to calculate its instantaneous slant-range, the new coordinate, denoted by $O_{prec} - x_{prec}y_{prec}z_{prec}$, is built, where x_{prec}*-axis* is parallel to the horizontal axis of antenna panel, y_{prec}*-axis* refers to the missile body axis, and z_{prec}*-axis* is determined by the right-hand rule, as shown in Fig. 5.

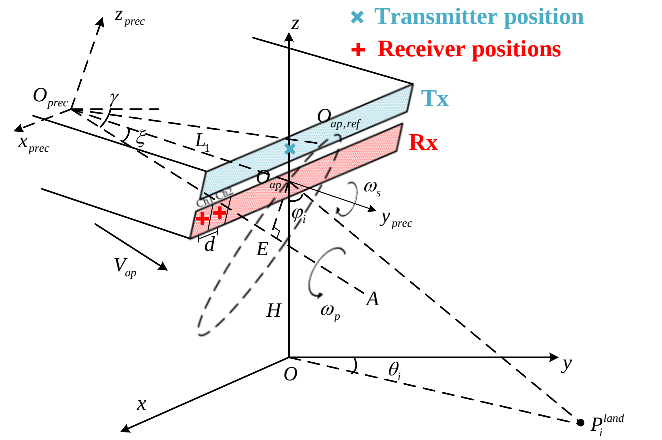

Fig. 5. The sketch-map of the new coordinate system of O_{prec}-$x_{prec}y_{prec}z_{prec}$.

Obviously, according to Fig. 5, the instantaneous slant-range calculation corresponding to P_i^{land} in $O_{prec} - x_{prec}y_{prec}z_{prec}$ coordinate can effectively eliminate the missile spinning and coning motion influences. After performing the coordinate system transformation with respect to the new coordinate $O_{prec} - x_{prec}y_{prec}z_{prec}$ and the ground reference coordinate *O-xyz*, the 3-D coordinate values of the ground scatterer P_i^{land} in $O_{prec} - x_{prec}y_{prec}z_{prec}$ coordinate can be given by

$$\begin{pmatrix} x_{P_{i,prec}^{land}} \\ y_{P_{i,prec}^{land}} \\ z_{P_{i,prec}^{land}} \end{pmatrix} = M_{trA}\left[\begin{pmatrix} x_{P_i^{land}} \\ y_{P_i^{land}} \\ z_{P_i^{land}} \end{pmatrix} - coor_{tran}\right] \tag{4}$$

where the detailed deduction and the definition of M_{trA} and $coor_{tran}$ are depicted in Appendix B.

In the following section, the instantaneous two-way slant-range of P_i^{land} is calculated based on (4).

b) Double-Way Slant-Range History Calculation

For the arbitrary ground scatterer P_i^{land}, the instantaneous two-way slant-range related to the nth received channel is

$$R_{n,i}^{land}\left(t_m\right) = \frac{1}{2}\left[R_T\left(t_m\right) + R_{R,n}\left(t_m\right)\right] \tag{5}$$

where $R_T\left(t_m\right)$ and $R_{R,n}\left(t_m\right)$ denote, respectively, the transmitted and received slant-range histories. In O_{prec}-$x_{prec}y_{prec}z_{prec}$ coordinate, $R_T\left(t_m\right)$ is

$$R_T\left(t_m\right) = \sqrt{R_{T,x_{prec}}^2\left(t_m\right) + R_{T,y_{prec}}^2\left(t_m\right) + R_{T,z_{prec}}^2\left(t_m\right)} \tag{6}$$

where $R_{T,x_{prec}}\left(t_m\right)$, $R_{T,y_{prec}}\left(t_m\right)$, and $R_{T,z_{prec}}\left(t_m\right)$ denote, respectively, the relative distances between the ground scatterer P_i^{land} and the transmitted channel center position along x_{prec}*-axis*, y_{prec}*-axis*, and z_{prec}*-axis* in O_{prec}-$x_{prec}y_{prec}z_{prec}$

Accepted Manuscript
Version of record at: https://doi.org/10.1109/TAES.2022.3147136

coordinate. The velocity components of transmitted channel center include the translational velocity V_{ap} and the coning velocity V_p, where the direction of V_{ap} coincides with $\overline{O_{prec}A}$ and the direction of the coning velocity V_p, denoted by $\overrightarrow{n_p}$, is perpendicular to $\overline{O_{ap}E}$ and $\overline{O_{prec}A}$. It should be noted that the spinning motion will not affect the position of transmitted channel position.

In addition, the received slant-range corresponding to the nth received channel is noted as

$$R_{R,n}\left(t_m\right)=\sqrt{R_{R,n,x_{prec}}^2\left(t_m\right)+R_{R,n,y_{prec}}^2\left(t_m\right)+R_{R,n,z_{prec}}^2\left(t_m\right)} \tag{7}$$

where $R_{R,n,x_{prec}}\left(t_m\right)$, $R_{R,n,y_{prec}}\left(t_m\right)$, and $R_{R,n,z_{prec}}\left(t_m\right)$ denote, respectively, the relative distances between the ground scatterer P_i^{land} and the nth received channel position along x_{prec}-*axis*, y_{prec}-*axis*, and z_{prec}-*axis*.

Combining the transmitted slant-range in (6) with the received slant-range in (7), the two-way instantaneous slant-range associated with the nth received channel is finally expressed as (the detailed derivation is shown in Appendix C):

$$R_{n,i}^{land}\left(t_m\right)\approx R_{0,i}+\frac{X}{2R_{0,i}}t_m+\frac{Y}{4R_{0,i}}t_m^2+\frac{d_n^2-2x_{P_{i,prec}^{land}}d_n}{4R_{0,i}} \tag{8}$$

where the expressions of X and Y are shown in (C17) and (C18).

Obviously, it can be seen from (C17) (see Appendix C) that X contains the complex disturbance terms related to the 3-D velocity components, which indicates that the clutter Doppler frequency no longer maintaining a one-to-one correspondence with the spatial cone angle, aggravating the clutter non-stationary characteristics.

B. Transmitted/Received Array Pattern Calculation

Assume that the antenna array consists of M_0 rows and N_0 columns of transmit-receive (T/R) modules, and T/R modules are arranged equally spaced. The physical interval between adjacent rows is d_{row} and between adjacent columns is d_{col}. Suppose that the received azimuth antennas are uniformly divided into N sub-channels. In order to calculate the array pattern, the elevation angle and azimuth angle of a ground scatterer relative to the antenna panel should be calculated.

1) Angle Conversion under Forward-looking Mode with Level Flight

When the missile platform works in the forward-looking mode of level flight, the relationships between the ground scattering point's elevation angle and azimuth angle relative to the antenna panel and its elevation angle and azimuth angle in the ground coordinate system are given as follows:

$$\varphi_{ap}=\varphi_i,\theta_{ap}=\theta_i+\frac{\pi}{2} \tag{9}$$

where φ_{ap} and φ_i denote the elevation angles relative to the antenna panel coordinate (as shown in Fig. 6.) and the ground reference coordinate, respectively, θ_{ap} and θ_i correspond to the azimuth angles in the antenna panel coordination and the ground reference coordinate, respectively.

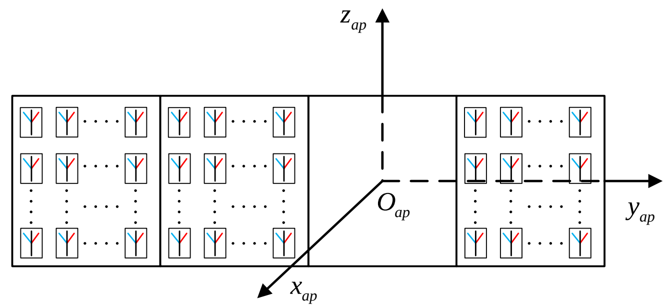

Fig. 6. The sketch-map of the antenna panel coordinate system of O_{ap}-$x_{ap}y_{ap}z_{ap}$.

2) Angle Conversion under Forward-looking Mode with Diving Flight

The coordinates of a scattering point P_i^{land} in the ground coordinate system can be represented as:

$$\begin{pmatrix}x_{P_i^{land}}\\ y_{P_i^{land}}\\ z_{P_i^{land}}\end{pmatrix}=\begin{pmatrix}R_{0,i}\sin\varphi_i\sin\theta_i\\ R_{0,i}\sin\varphi_i\cos\theta_i\\ 0\end{pmatrix} \tag{10}$$

According to (10), when the missile-borne radar works in the diving and forward-looking mode, the coordinate transformation relationship from the ground reference coordinate to the antenna panel coordinate is obtained as:

$$\begin{pmatrix}x_{P_{i,ap}^{land}}\\ y_{P_{i,ap}^{land}}\\ z_{P_{i,ap}^{land}}\end{pmatrix}=\begin{pmatrix}R_{0,i}\sin\varphi_i\cos\theta_i\cos\gamma+R_{0,i}\cos\varphi_i\sin\gamma\\ -R_{0,i}\sin\varphi_i\sin\theta_i\\ R_{0,i}\sin\varphi_i\cos\theta_i\sin\gamma-R_{0,i}\cos\varphi_i\cos\gamma\end{pmatrix} \tag{11}$$

Therefore, the elevation angle and azimuth angle relative to the antenna panel coordinate can be, respectively, noted as:

$$\varphi_{ap}=\arccos\left(\cos\varphi_i\cos\gamma-\sin\varphi_i\cos\theta_i\sin\gamma\right) \tag{12}$$

$$\theta_{ap}=\arctan\left(-\frac{\sin\varphi_i\cos\theta_i\cos\gamma+\cos\varphi_i\sin\gamma}{\sin\varphi_i\sin\theta_i}\right) \tag{13}$$

3) Angle Conversion under Diving and Forward-looking Mode with Spinning and Coning Motions

For a diving and forward-looking missile-borne radar, according to Section II.A, the 3-D coordinate of P_i^{land} in the antenna panel coordinate can be noted as

$$\begin{pmatrix}x_{P_{i,ap}^{land}}\\ y_{P_{i,ap}^{land}}\\ z_{P_{i,ap}^{land}}\end{pmatrix}=\begin{pmatrix}\cos 90^\circ & \sin 90^\circ & 0\\ -\sin 90^\circ & \cos 90^\circ & 0\\ 0 & 0 & 1\end{pmatrix}\left\{M_{trA}\left[\begin{pmatrix}R_{0,i}\sin\varphi_i\sin\theta_i\\ R_{0,i}\sin\varphi_i\cos\theta_i\\ 0\end{pmatrix}-\begin{pmatrix}-L_1\sin\xi\sin\alpha_0\\ -L_1\cos\left(\gamma-\xi\right)+L_1\sin\xi\sin\gamma\left(1-\cos\alpha_0\right)\\ H+L_1\sin\xi\cos\gamma\left(1-\cos\alpha_0\right)+L_1\sin\left(\gamma-\xi\right)\end{pmatrix}\right]-\begin{pmatrix}0\\ L_1\\ 0\end{pmatrix}\right\} \tag{14}$$

Accepted Manuscript
Version of record at: https://doi.org/10.1109/TAES.2022.3147136

Therefore, the elevation angle and azimuth angle relative to the antenna panel can be, respectively, expressed as:

$$\varphi_{ap}=\arccos\left(\frac{-z_{P_{i,ap}^{land}}}{R_{0,i}}\right),\theta_{ap}=\arctan\left(\frac{x_{P_{i,ap}^{land}}}{y_{P_{i,ap}^{land}}}\right) \tag{15}$$

4) Transmitted-Received Antenna Pattern Calculation

Assume that the elevation angle and azimuth angle of the beam center point are, respectively, denoted by $\varphi_{ap,b}$ and $\theta_{ap,b}$ in the antenna panel coordinate system. Then the transmitted pattern synthesized along range dimension is:

$$\begin{aligned}&f_{t,col}\left(\varphi_{ap}\right)\\&=\sum_{m_0=1}^{M_0}\omega_{m_0}\exp\left[\frac{j2\pi d_{col}}{\lambda}\left(m_0-1\right)\left(\cos\varphi_{ap}-\cos\varphi_{ap,b}\right)\right]\end{aligned} \tag{16}$$

where $\omega_{m_0}\left(m_0=1,2,\cdots,M_0\right)$ is the transmitted weight of column subarray, M_0 is the number of T/R modules in rows, λ is the wave length of transmitted signal, and φ_{ap} represents the elevation angles relative to the antenna panel coordinate according to (9), (12), and (15).

The transmitted pattern synthesized along azimuth dimension can be obtained as:

$$\begin{aligned}&f_{t,row}\left(\varphi_{ap},\theta_{ap}\right)\\&=\sum_{n_0=1}^{N_0}\omega_{n_0}\exp\left[\frac{j2\pi d_{row}}{\lambda}\left(n_0-1\right)\sin\varphi_{ap}\cos\theta_{ap}\right]\\&\quad\times\exp\left[-\frac{j2\pi d_{row}}{\lambda}\left(n_0-1\right)\sin\varphi_{ap,b}\cos\theta_{ap,b}\right]\end{aligned} \tag{17}$$

where $\omega_{n_0}\left(n_0=1,2,\cdots,N_0\right)$ is the weight of row subarray, N_0 denotes the number of T/R modules in columns, φ_{ap} and θ_{ap} can obtained from (9) to (15).

Then the synthetic transmitted array pattern can be expressed as:

$$\begin{aligned}f_t\left(\varphi_{ap},\theta_{ap}\right)&=\sum_{m_0=1}^{M_0}\omega_{m_0}\exp\left[\frac{j2\pi d_{col}}{\lambda}\left(m_0-1\right)\left(\cos\varphi_{ap}-\cos\varphi_{ap,b}\right)\right]\\&\quad\times\sum_{n_0=1}^{N_0}\omega_{n_0}\exp\left[\frac{j2\pi d_{row}}{\lambda}\left(n_0-1\right)\sin\varphi_{ap}\cos\theta_{ap}\right]\\&\quad\times\exp\left[-\frac{j2\pi d_{row}}{\lambda}\left(n_0-1\right)\sin\varphi_{ap,b}\cos\theta_{ap,b}\right]\end{aligned} \tag{18}$$

For the same reason, the received pattern with respect to a sub-channel is expressed as follow:

$$\begin{aligned}&f_{r,sub}\left(\varphi_{ap},\theta_{ap}\right)\\&=\sum_{m_0=1}^{M_0}\tilde{\omega}_{m_0}\exp\left[\frac{j2\pi d_{col}}{\lambda}\left(m_0-1\right)\left(\cos\varphi_{ap}-\cos\varphi_{ap,b}\right)\right]\\&\quad\times\sum_{n_0=1}^{N_0/N}\tilde{\omega}_{n_0}\exp\left[\frac{j2\pi d_{row}}{\lambda}\left(n_0-1\right)\sin\varphi_{ap}\cos\theta_{ap}\right]\\&\quad\times\exp\left[-\frac{j2\pi d_{row}}{\lambda}\left(n_0-1\right)\sin\varphi_{ap,b}\cos\theta_{ap,b}\right]\end{aligned} \tag{19}$$

where $\tilde{\omega}_{m_0}\left(m_0=1,2,\cdots M_0\right)$ and $\tilde{\omega}_{n_0}\left(n_0=1,2,\cdots,N_0/N\right)$ represent the weight values of received pattern along range and azimuth dimensions, respectively. It should be noted that compared with the transmitted antenna pattern in (18), the azimuth main-lobe width of the received antenna pattern with respect to a sub-channel is dramatically broadened due to the antenna panel division, which indicates that the clutter level is mainly modulated by the transmitted antenna pattern.

In the following, based on the above theoretical analysis results, a simulation example about transmitted and received array patterns is given. In this simulation, the missile-borne radar with complex motions including diving, spinning, and coning is considered, where the received antenna panel along azimuth direction is uniformly divided into N sub-channels. The other radar system parameters are listed in Table 1:

Table 1 Radar system parameters

Radar frequency	30 GHz
Number of azimuth channels	8
Elevation angle of beam center	60°
Azimuth angle of beam center	0°
Diving angle	15°
Spinning angle	30°
Coning angle	40°
ξ	5°
Transmitted azimuth and elevation sidelobes	-13.4 dB/-13.4 dB (Rectangle weighting)
Received azimuth and elevation sidelobes	-40 dB/-20 dB (Tylor weighting)

Accepted Manuscript
Version of record at: https://doi.org/10.1109/TAES.2022.3147136

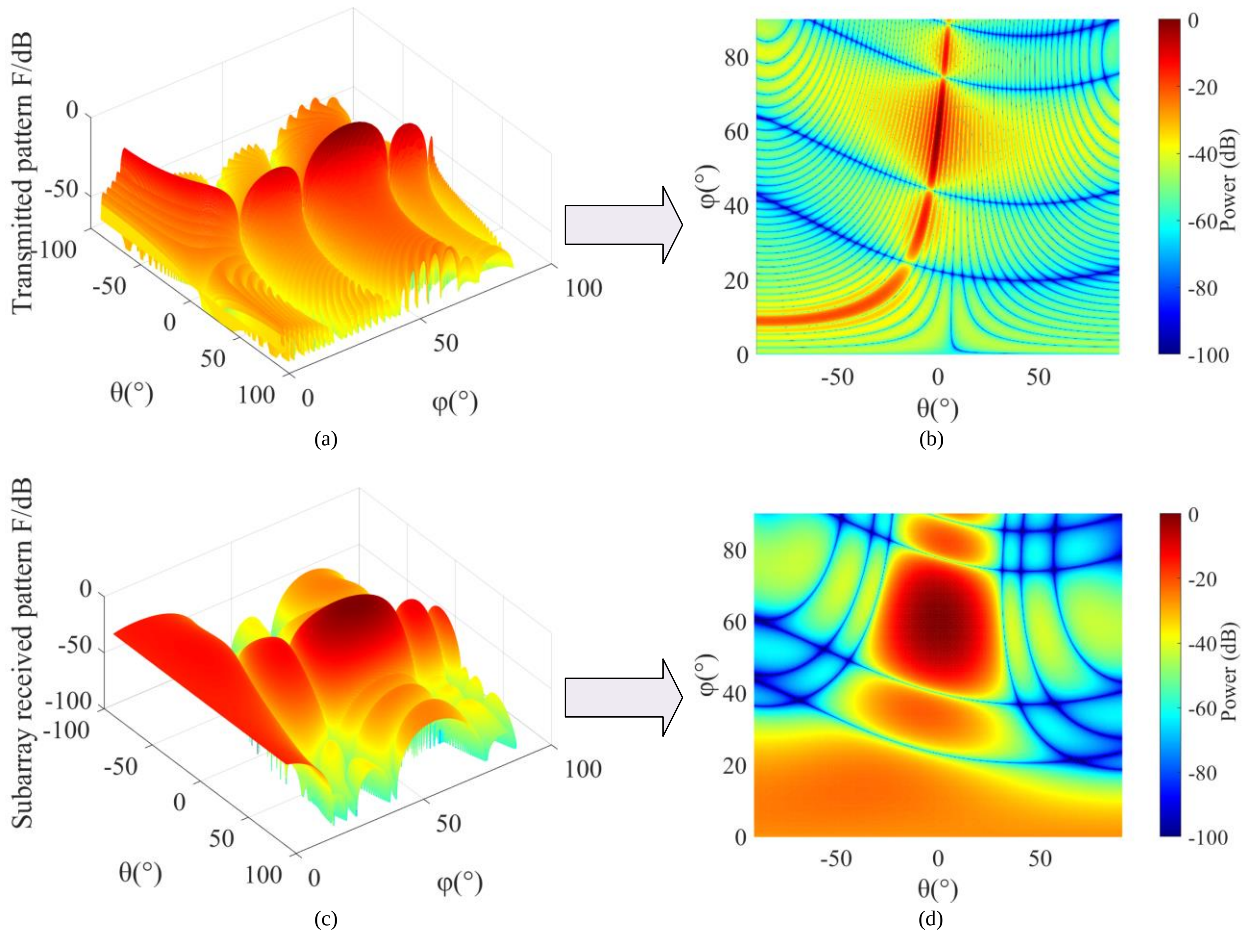

Fig. 7. Transmitted and received antenna pattern simulation results. (a) and (b) Transmitted antenna pattern in the ground coordinate system. (c) and (d) Sub-channel received antenna pattern in the ground coordinate system.

Fig. 7(a) and (b) show the transmitted and sub-channel received patterns in the ground coordinate system, from which it can be observed that because of missile-borne platform complex motions, such as diving, spinning, and coning, the main-lobe antenna patterns of transmitter and receiver are severely distorted, with the main-lobe pattern variation trend depending on the elevation angle, indicating that the range dependence of observed clutter will be present due to the non-ideal platform motions. In addition, compared with Fig. 7(a) and (b), the azimuth main-lobe width of the received antenna pattern provided in Fig. 7(c) and (d) is significantly broadened, as forecast by (18) and (19).

C. Range and Azimuth Resolution Calculation

In the procedure of ground clutter signal modeling, the 2-D ground clutter block partition is a key step. In practice, the ground clutter is usually divided into an amount of small patches according to the radar range and azimuth resolutions. Usually, for a missile-borne radar, the ground resolution along range dimension is $\Delta R_{ground} = \dfrac{c}{2B\sin(\varphi_i)}$ [52], where B is the bandwidth of the transmitted pulse signal and φ_i denotes the elevation angle of scatterer. In the following, the azimuth resolutions in different motion statements are deduced.

1) Azimuth Resolution Calculation of a Forward-looking Missile-borne Radar with Level Flight

For a forward-looking missile-borne radar with the platform velocity of V_{ap}, according to (2), Doppler frequency of a static clutter component with the elevation angle of φ_i and azimuth angle of θ_i is given by

$$f_d = \frac{2V_{ap}\sin\varphi_i\cos\theta_i}{\lambda} \tag{20}$$

Assuming that K radar pulses are transmitted, the relationship between the Doppler resolution and azimuth resolution can be expressed as

$$\Delta f_d \approx \frac{2V_{ap}\cos\varphi_i\cos\theta_i}{\lambda}\Delta\varphi - \frac{2V_{ap}\sin\varphi_i\sin\theta_i}{\lambda}\Delta\theta \tag{21}$$

where $PRF = 1/PRT$ is the pulse repetition frequency. Obviously, for a fixed elevation angle of φ_i, the azimuth resolution of a forward-looking missile-borne radar with level flight can be noted as:

$$\Delta x \approx \frac{R_{0,i}\lambda \cdot PRF}{2KV_{ap}\sin\varphi_i\sin\theta_i} \tag{22}$$

Accepted Manuscript
Version of record at: https://doi.org/10.1109/TAES.2022.3147136

Obviously, it can be seen from (22) that for the ground scatterers located around the regions of $\theta_i = 0$, the radar azimuth resolution significantly deteriorates.

2) Azimuth Resolution Calculation of a Forward-looking Missile-borne Radar with Diving Flight

For a forward-looking missile-borne radar with a diving angle of γ, according to (3), Doppler frequency of a stationary ground scatterer with the elevation angle of φ_i and the azimuth angle of θ_i can be noted as:

$$f_d = \frac{2V_{ap}\left(\sin\varphi_i\cos\theta_i\cos\gamma + \cos\varphi_i\sin\gamma\right)}{\lambda} \tag{23}$$

For the same reason, the resolution of Doppler frequency can be obtained as follows:

$$\begin{aligned}\Delta f_d \approx & -\frac{2V_{ap}\sin\varphi_i\sin\theta_i\cos\gamma}{\lambda}\cdot\Delta\theta \\ & + \frac{2V_{ap}\left(\cos\varphi_i\cos\theta_i\cos\gamma - \sin\varphi_i\sin\gamma\right)}{\lambda}\cdot\Delta\varphi\end{aligned} \tag{24}$$

When φ_i is a fixed angle, the azimuth resolution of a forward-looking missile-borne radar with diving flight can be expressed as:

$$\Delta x = \frac{R_{0,i}\lambda\cdot PRF}{2KV_{ap}\sin\varphi_i\sin\theta_i\cos\gamma} \tag{25}$$

Obviously, compared with (22), it can be observed from (25) that the azimuth resolution further worsens because of the presence of diving angle γ.

3) Azimuth Resolution Calculation of a Forward-looking Missile-borne Radar with Diving Flight and Spinning/Coning Motions

When the spinning and conning motions are considered, according to (8), Doppler frequency of a static ground scatterer at the elevation angle of φ_i and azimuth angle of θ_i can be expressed as:

$$f_d = -\frac{X}{\lambda R_{0,i}} \tag{26}$$

where X (see Appendix C) is a function of the elevation angle of φ_i, azimuth angle of θ_i, spinning angle of β_0, and coning angle of α_0. Then Doppler resolution can be obtained as:

$$\Delta f_d \approx -\frac{1}{\lambda R_{0,i}}\left(\frac{\partial X}{\partial\varphi_i}\Delta\varphi + \frac{\partial X}{\partial\theta_i}\Delta\theta + \frac{\partial X}{\partial\alpha_0}\Delta\alpha + \frac{\partial X}{\partial\beta_0}\Delta\beta\right) \tag{27}$$

Based on (27), the azimuth resolution in this case can be finally noted as follows:

$$\Delta x_i \approx \left|\frac{R_{0,i}^2\lambda\cdot PRF}{K\cdot\partial X/\partial\theta_i}\right| \tag{28}$$

As it is apparent, different from the azimuth resolution calculation results in (22) and (25), the azimuth resolution in (28) rapidly degrades because of the platform complex motions.

D.Multichannel Signal Modeling in a Missile-borne Radar System

Assume that the missile-borne radar adopts the linear frequency modulation (LFM) signal as the transmitted signal waveform, that is

$$s(t) = rect\left(\frac{t}{T_e}\right)\exp\left(j2\pi f_0 t + j\pi\mu t^2\right) \tag{29}$$

where $rect(\cdot)$ denotes the rectangular window, f_0 is the carrier frequency, T_e represents the pulse duration of transmitted signal, $\mu = \frac{B}{T_e}$ is the chirp rate, and B corresponds to the signal bandwidth. Then, after range pulse compression, for the ground scatterer P_i in the range ring corresponding to the slant-range of r, the echo signal received by the *n*th azimuth channel of a missile-borne radar can be noted as:

$$S_{n,i}(r,t_m) = A_{r,i}\,\mathrm{sinc}\left\{\frac{2B}{c}\left[r - R_{n,i}(t_m)\right]\right\}\exp\left[-\frac{j4\pi}{\lambda}R_{n,i}(t_m)\right] \tag{30}$$

where $R_{n,i}(t_m)$ represents the instantaneous slant-range between the clutter point P_i and the radar platform, as discussed in Section II.A. $A_{r,i}$ denotes the echo signal amplitude in r-t_m domain. Assuming that the clutter signal located at the range ring with the slant-range of *r* is composed of N_c clutter blocks, the total echo signal received by the *nth* azimuth channel is given by

$$\begin{aligned}S_n(r,t_m) &= \sum_{i=1}^{N_c} S_{n,i}(r,t_m) \\ &= \sum_{i=1}^{N_c} A_{r,i}\,\mathrm{sinc}\left\{\frac{2B}{c}\left[r - R_{n,i}(t_m)\right]\right\} \\ &\quad \times\exp\left[-\frac{j4\pi}{\lambda}\left(R_{0,i} + \frac{X}{2R_{0,i}}t_m + \frac{Y}{4R_{0,i}}t_m^2 + \frac{d_n^2 - 2x_{P_{i,prec}^{land}}d_n}{4R_{0,i}}\right)\right]\end{aligned} \tag{31}$$

Considering that the beam dwell time in a missile-borne radar system is relatively short, the quadratic term in (31) can be approximately compensated by using the priori radar system parameters. Then, after performing the azimuth FFT, one has

$$\begin{aligned}S_n(r, f_a) = \sum_{i=1}^{N_c}\sigma_{r,i}\,\mathrm{sinc}\left\{\frac{2B}{c}\left[r - R_{n,i}(f_a)\right]\right\} \\ \times\exp\left[-\frac{j4\pi}{\lambda}\left(R_{0,i} + \frac{d_n^2 - 2x_{P_{i,prec}^{land}}d_n}{4R_{0,i}}\right)\right] \\ \times\mathrm{sinc}\left[T_a\left(f_a + \frac{X}{\lambda R_{0,i}}\right)\right]\end{aligned} \tag{32}$$

Accepted Manuscript
Version of record at: https://doi.org/10.1109/TAES.2022.3147136

where $\sigma_{r,i}$ is the signal amplitude of the ith clutter block in r-f_a domain, and f_a denotes the Doppler frequency variable. According to (C17) in Appendix C, one can see that the ith clutter block will be located at the Doppler frequency of

$$f_a^{land} = \frac{\overrightarrow{O_{ap}P_{i,prec}^{land}}\left(\overrightarrow{V_{ap}}+\overrightarrow{V_p}\right)+\overrightarrow{O_nP_{i,prec}^{land}}\left(\overrightarrow{V_{ap}}+\overrightarrow{V_{pn}}+\overrightarrow{V_s}\right)}{\lambda R_{0,i}} \quad (33)$$

Obviously, it is observed from (33) that the clutter Doppler frequency is not only related to the elevation angle φ_i and azimuth angle θ_i, but also related to the diving angle γ, the spinning angle β_0, and the conning angle α_0. Therefore, the missile-borne platform complex motions will make the clutter Doppler frequency and spatial angular frequency no longer keep the one-to-one correspondence, which indicates that the severe non-stationary phenomenon of ground clutter in a missile-borne radar system will appear in turn.

III. Robust Multi-Channel Clutter Suppression

A. Adaptive Angle Doppler Compensation

According to the multi-channel signal model in Section II, for a missile-borne radar system in a forward-looking mode with complex motions, such as diving, spinning, and coning, one can see that, the received radar returns of ground scatterers show the severe range-dependence. At this time, if the conventional 2-D space-time adaptive processing (STAP) technique is carried out directly, the STAP performance will deteriorate rapidly because of the lack of i.i.d. samples. Therefore, to improve the subsequent clutter spatial filtering ability, the effective clutter pre-processing steps should be implemented in order to provide the enough i.i.d. training samples in the subsequent spatial filtering.

Based on the clutter returns in (31), the normalized clutter Doppler centers along every range gate can be estimated by applying the temporal correlation operation, that is

$$\overline{f}_{t,r} = E_n\left\{\frac{\left\{\sum_{k=1}^{K-1} angle\left[S_n\left(r,k\cdot PRT\right)S_n^*\left(r,\left(k-1\right)\cdot PRT\right)\right]\right\}}{2\pi\left(K-1\right)}\right\} \quad (34)$$

where $S_n\left(r,kPRT\right)$ is given in (31) and $E_n\left[\cdot\right]$ represents the mathematical expectation operation along the spatial channel. Then the time domain compensation matrix $T_{t,r}$ can be devised as:

$$T_{t,r} = \begin{bmatrix} 1 & 0 & \cdots & 0 \\ 0 & \exp\left[j2\pi\cdot\Delta f_t\right] & \cdots & 0 \\ \vdots & \vdots & \ddots & \vdots \\ 0 & 0 & \cdots & \exp\left[j2\pi\left(K-1\right)\cdot\Delta f_t\right] \end{bmatrix} \quad (35)$$

where K represents the number of transmitted pulses, and $\Delta f_t = \overline{f}_{t,r} - \overline{f}_{t,0}$ with $\overline{f}_{t,0}$ corresponding to the normalized Doppler frequency with respect to the reference range unit.

As for the range dependence compensation, the traditional methods include the 1-D spectrum compensation methods, such as Doppler warping (DW) [53] method, which compensate the dependence only along the Doppler domain and the compensation performance deteriorates when the angle frequency is dependent. And the 2-D compensation methods, such as angle-Doppler compensation method (ADC) [54], space-time interpolation (STINT) [55], High order Doppler warping method (HODW) [56], etc., require a *priori* system information to determine the compensation function. However, in a missile-borne system, the radar system parameters and the platform motion parameters may not be accurately obtained. To solve this problem, some adaptive clutter space-time two-dimensional compensation methods are proposed in recent years, such as adaptive angle-Doppler compensation (A^2DC) method [57], derivative based updating (DBU) method [58], nonlinear prediction for inverse covariance matrix (NI-PICM) [59], etc., where the A^2DC method is a typical spectrum compensation method and is independent of priori system parameters. However, the two-dimensional sliding window processing will lose the precious time-domain pulse information and the spatial-domain aperture information. Especially for a missile borne radar system, due to the limitation of the platform volume, the number of received channels along azimuth dimension is small, and the loss of a half of the spatial apertures will severely reduce the spatial resolution. Therefore, in a missile borne radar system the angle-Doppler dependent errors may not be precisely compensated by using the A^2DC method. To deal with this issue, motivated by the previous works, after performing the Doppler center estimation by using the correlation method in (34) and (35), the IAA method [32]-[35] is applied to accomplish the resolution estimation of spatial frequency center, which does not require the priori system parameters existed in the methods in [53]-[56] and can effectively offset the reduction of spatial resolution existed in A^2DC. The main steps of IAA are summarized in Table 2.

Table 2 Main steps of the spatial spectrum center estimation

Initialize the range $r = R_{\min}$.

Repeat

Initialize the covariance matrix $R_{X_0,r}$ of the received data matrix X_r:

$$R_{X_0,r} = X_r X_r^H / K \quad (36)$$

where:

$$X_r = \begin{bmatrix} S_1\left(r,PRT\right) & S_1\left(r,2\cdot PRT\right) & \cdots & S_1\left(r,K\cdot PRT\right) \\ S_2\left(r,PRT\right) & S_2\left(r,2\cdot PRT\right) & \cdots & S_2\left(r,K\cdot PRT\right) \\ \vdots & \vdots & \cdots & \vdots \\ S_N\left(r,PRT\right) & S_N\left(r,2\cdot PRT\right) & \cdots & S_N\left(r,K\cdot PRT\right) \end{bmatrix} \quad (37)$$

Set the number of spatial scanning points as J, and accordingly construct the equivalent spatial steering matrix as follows:

$$A\left(f_s\right) = \left[a\left(f_{s,1}\right), a\left(f_{s,2}\right), \cdots, a\left(f_{s,J}\right)\right] \quad (38)$$

where $a\left(f_{s,j}\right) = \left[1, \exp\left(j2\pi f_{s,j}\right), \cdots, \exp\left(j2\pi\left(N-1\right)f_{s,j}\right)\right]^T$.

Initialize the power matrix P as:

$$P = diag\left\{P_1, P_2, \cdots, P_j, \cdots, P_J\right\} \quad (39)$$

where:

Accepted Manuscript
Version of record at: https://doi.org/10.1109/TAES.2022.3147136

$$P_j = \frac{a^H\left(f_{s,j}\right) R_{X_0,r} a\left(f_{s,j}\right)}{\left[a^H\left(f_{s,j}\right) a\left(f_{s,j}\right)\right]^2}, \quad j = 1,2,\cdots,J \tag{40}$$

Repeat

Step 1) Update the covariance matrix according to the power matrix:

$$R_{X,r} = A\left(f_s\right) P A^H\left(f_s\right) \tag{41}$$

Step 2) Calculate the optimal weight vector:

$$\omega_{opt,j} = \frac{R_{X,r}^{-1} a\left(f_{s,j}\right)}{a^H\left(f_{s,j}\right) R_{X,r}^{-1} a\left(f_{s,j}\right)} \tag{42}$$

and update the *jth* diagonal element of the power matrix P as

$$P_j = \omega_{opt,j}^H R_{X_0,r} \omega_{opt,j}, \quad j = 1,2,\cdots,J \tag{43}$$

Until the repetition number reaches the preset iteration number.

Update the next range gate as $r = R_{\min} + \dfrac{c}{2F_s}$ and repeat the above steps.

Until all the range units are calculated.

Finally, the spatial frequency center in a given range can be precisely estimated according to the peak position of the power matrix $\hat{P}$.

Considering that the Doppler frequency and spatial frequency centers in different range bins estimated by autocorrelation method and IAA may be miscalculated due to the weak clutter intensity, the global least square (GLS) [36] is applied to correct some outliers from these angle-Doppler center estimation results with respect to different range gates. Specifically, the Doppler frequencies of clutter components in adjacent range units exhibit the small differences. However, some burrs will occur due to the random noise signal, the weak clutter scatterers, the channel amplitude/phase error, etc., which may disturb the final 2-D spectrum compensation results. Therefore, to deal with these issues, when the estimated spatial and Doppler frequency center errors exceed a certain threshold, their contributions to the final fitting results by GLS will be discarded so as to further improve the 2-D spectrum compensation precision in a missile-borne radar system.

For the same reason, assuming that the estimated normalized spatial frequency center is $\overline{f}_{s,r}$, then for the training samples with the slant-range of r, the angle-dependence compensation matrix $T_{s,r}$ can be constructed as follows:

$$T_{s,r} = \begin{bmatrix} 1 & 0 & \cdots & 0 \\ 0 & \exp\left[j2\pi\cdot\Delta f_s\right] & \cdots & 0 \\ \vdots & \vdots & \ddots & \vdots \\ 0 & 0 & \cdots & \exp\left[j2\pi\left(N-1\right)\cdot\Delta f_s\right] \end{bmatrix} \tag{44}$$

where $\Delta f = \overline{f}_{s,r} - \overline{f}_{s,0}$ with $\overline{f}_{s,0}$ being the normalized spatial frequency center of the reference range cell.

Then, based on (35) and (44), the 2-D angle-Doppler compensation matrix for the non-stationary clutter in a missile-borne radar system can be expressed as:

$$\begin{aligned} T_r &= T_{t,r} \otimes T_{s,r} \\ &= diag\left\{ \begin{array}{l} 1, \exp\left[j2\pi\left(\overline{f}_{t,r} - f_{t,0}\right)\right], \\ \quad \cdots, \exp\left[j2\pi\left(K-1\right)\left(\overline{f}_{t,r} - f_{t,0}\right)\right] \end{array} \right\} \\ &\quad \otimes diag\left\{ \begin{array}{l} 1, \exp\left[j2\pi\left(\overline{f}_{s,r} - f_{s,0}\right)\right], \\ \quad \cdots, \exp\left[j2\pi\left(N-1\right)\left(\overline{f}_{s,r} - f_{s,0}\right)\right] \end{array} \right\} \end{aligned} \tag{45}$$

where $\otimes$ represents the Kronecker product. Finally, the compensated clutter data can be given by

$$S_{TC-IAA,r} = T_r^H \begin{bmatrix} S_1\left(r, PRT\right), S_2\left(r, PRT\right), \cdots, S_N\left(r, PRT\right) \\ , \cdots S_1\left(r, K\cdot PRT\right), \cdots, S_N\left(r, K\cdot PRT\right) \end{bmatrix}^T \tag{46}$$

where $S_{TC-IAA,r}$ is the multi-channel echo data after adaptive compensation of the range ring with the slant-range of *r*. According to $S_{TC-IAA,r}$, the multi-channel data in $r-t_m$ domain can be rearranged as $S_{n,Comp}\left(r, t_m\right)$.

Therefore, by using the correlation method and the IAA based spectrum estimation method, the 2-D angle-Doppler dependence errors can be precisely estimated and compensated, which is the rational of this paper for the 2-D clutter spectrum compensation in a multi-channel missile-borne radar configuration.

B. Multi-channel Clutter Cancellation By TSWSP

After compensating the non-stationary characteristics of the radar echo data according to Section III.A, a modified subspace projection (SP) based technique, i.e., TSWSP, is applied to realize the clutter cancellation.

The TSWSP method proposed in this paper is mainly based on the following considerations:

1) On one hand, the clutter rejection method based on subspace projection does not require the inversion of covariance matrix, and thus has extremely low computational complexity, which can satisfy the real-time processing requirement and is conducive to hardware implementation in a multi-channel missile-borne radar system;

2) Another aspect is the purpose of improving the clutter rejection performance. As for the proposed TSWSP method, due to the fact that multiple groups of data can be obtained by applying the time-domain sliding window processing, more equivalent spatial channels can be applied to participate in the spatial filtering. Therefore, the clutter space can be precisely fit by using the proposed method, and thus the projection matrix in clutter rejection procedure can be precisely reconstructed, resulting in the improved clutter rejection performance.

In the following, the main steps of TSWSP method are discussed.

According to the 2-D Doppler-angular error compensation signal in (46), after performing the K_m times of time-domain sliding window, K_m groups of time-domain echo data can be

Accepted Manuscript
Version of record at: https://doi.org/10.1109/TAES.2022.3147136

obtained, with the k_mth set of radar data in the nth azimuth received channel given by

$$S_{k_m,n}(r,t_m)=\begin{bmatrix} S_{n,Comp}(r,k_m\cdot PRT), \\ \cdots,S_{n,Comp}(r,(K-K_m+k_m)\cdot PRT) \end{bmatrix} \quad (47)$$

where $k_m = 1,2,\cdots K_m$. Obviously, after performing the azimuth FFT with respect to $S_{k_m,n}(r,t_m)$, the relationship between the $k_m th$ set and the first set of radar data in the range-Doppler domain can be expressed as:

$$S_{k_m,n}(r,f_a)=S_{1,n}(r,f_a)\exp\left[j2\pi(k_m-1)f_a\cdot PRT\right] \quad (48)$$

Construct the data vector X_{r,f_a} of the rth range unit as:

$$X_{r,f_a}=\left[X_1(r,f_a),\cdots,X_{k_m}(r,f_a),\cdots,X_{K_m}(r,f_a)\right]^T \quad (49)$$

where $X_{k_m}(r,f_a)=\left[S_{k_m,1}(r,f_a),\cdots,S_{k_m,N}(r,f_a)\right]$ is the range-Doppler domain data with respect to these N azimuth received channels of the k_mth group of time-domain sliding window data.

Obviously, X_{r,f_a} in (49) can be rewritten as:

$$X_{r,f_a}=\exp\left(j2\pi f_a\cdot PRT\cdot[0,\cdots,K_m-1]^{\mathrm{T}}\right)\otimes X_1(r,f_a) \quad (50)$$

Then, the clutter subspace matrix can be expressed as

$$P(f_a)=a_c\left(a_c^{\mathrm{H}}a_c\right)^{-1}a_c^{\mathrm{H}} \quad (51)$$

where a_c denotes the clutter equivalent spatial vector after performing the time-domain sliding window. When the missile-borne radar works in a side-looking configuration, according to (1), the equivalent spatial steering vector a_c can be noted as:

$$\begin{aligned} a_c &= \exp\left(j2\pi f_a\cdot PRT\cdot[0,1,\cdots K_m-1]^{\mathrm{T}}\right) \\ &\otimes\exp\left(\frac{j\pi f_a\cdot d}{V_{ap}}[0,1,\cdots,N-1]^{\mathrm{T}}\right) \end{aligned} \quad (52)$$

In practice, when the radar system works in a forward-looking mode, after the adaptive angle-Doppler clutter compensation, the spatial frequency center of each range cell is moved to the referenced spatial angular frequency $\bar{f}_{s,0}$. Then, according to (8), the clutter equivalent spatial vector in this case is modified as

$$\begin{aligned} a_c &= \exp\left(j2\pi f_a\cdot PRT\cdot[0,1,\cdots K_m-1]^{\mathrm{T}}\right) \\ &\otimes\exp\left(\frac{j2\pi x_{0,prec}d}{\lambda R_{0,i}}[0,1,2,...,N-1]^{\mathrm{T}}\right) \end{aligned} \quad (53)$$

where $x_{0,prec}$ is the $x\!-\!axis$ coordinate of the reference scatterer related to the given Doppler frequency.

Then based on (51) and (53), the clutter suppression weight vector can be calculated as

$$w(f_a)=\frac{\left[I_{NK_m\times NK_m}-P(f_a)\right]\tilde{s}_{target}}{\tilde{s}_{target}^H\left[I_{NK_m\times NK_m}-P(f_a)\right]\tilde{s}_{target}} \quad (54)$$

where $I_{NK_m\times NK_m}$ is the identity matrix with the size of $N\cdot K_m\times N\cdot K_m$, and $\tilde{s}_{target}$ is the modified steering vector of a target, i.e., $\tilde{s}_{target}=\exp\left(j2\pi f_a\cdot PRT\cdot[0,\cdots K_m-1]^{\mathrm{T}}\right)\otimes s_{target}$.

Therefore, the final clutter suppression result is given by

$$X_{res}(r,f_a)=w^{\mathrm{H}}(f_a)X_{r,f_a} \quad (55)$$

Obviously, compared with the traditional SP method, the proposed TSWSP method creates more sets of time-domain sliding window data to realize the subsequent spatial adaptive processing, significantly improve the clutter spatial filtering robustness, and exhibits low computational complexity and can be suitable for the relatively inhomogeneous scene compared with the conventional reduced-dimension STAP method.

The flow chart of the proposed clutter 2-D spectrum compensation and robust clutter suppression procedures is shown in Fig. 8.

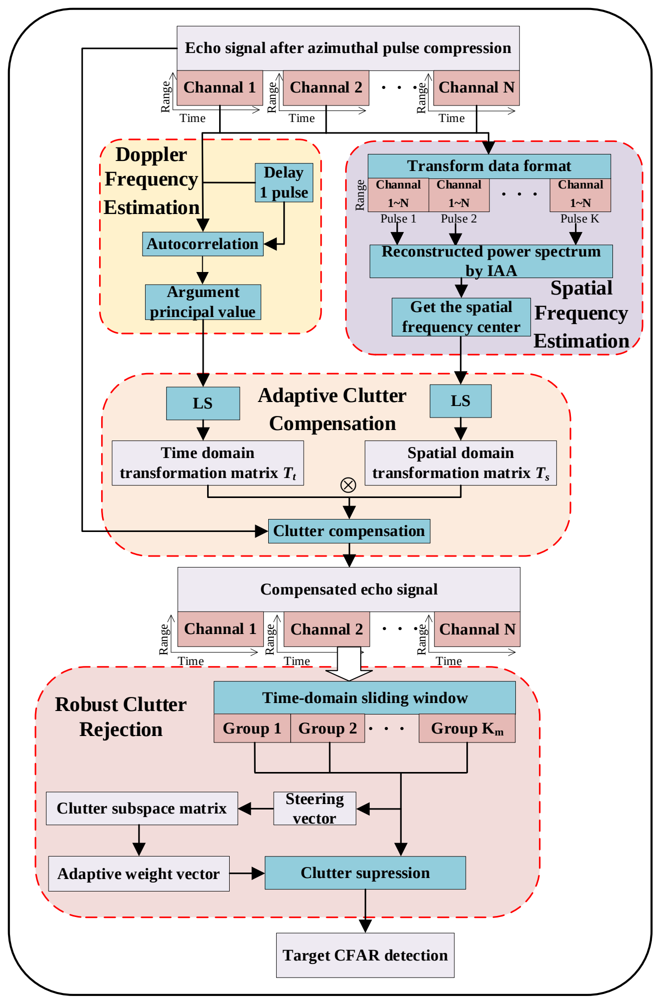

Fig. 8. Flow chart of the proposed 2-D clutter spectrum compensation and robust clutter suppression.

Accepted Manuscript
Version of record at: https://doi.org/10.1109/TAES.2022.3147136

IV. SIMULATED AND REAL DATA PROCESSING RESULTS

A. Missile-Borne Radar Clutter Analysis

In this section, the spatial-temporal characteristics of the missile-borne radar clutter with the configurations of horizontal side-looking, horizontal forward-looking, and diving forward-looking will be analyzed according to the simulation results. The simulation system parameters are shown in Table 3 to Table 5.

Table 3 Platform Parameters

Platform height	20 km
Platform velocity	1700 m/s

Table 4 Antenna Parameters

Azimuth/elevation antenna size	32 cm/4 cm
Transmitted antenna gain	30 dB
Received antenna gain	30 dB
Transmitted azimuth /elevation weighting	-13 dB/-13 dB (rectangle weighting)
Received azimuth /elevation weighting	-40 dB/-20 dB (Chebyshev weighting)

Table 5 Radar System Parameters

Carrier frequency	30 GHz
Pulse repetition frequency	20 kHz
Bandwidth	15 MHz
Number of received channels	8
Number of pulses in a CPI	64
Average transmitted power	2000 W
Noise factor	2 dB
System loss	11 dB

1) Horizontal Side-Looking Clutter Spectrum Analysis

According to the radar equation, the clutter-to-noise ratio (CNR) can be expressed as

$$CNR = \frac{P_{av} T_a G_t G_r \lambda^2 \Delta R_{ground} \Delta x B \sigma^0}{(4\pi)^3 R_0^4 k T_0 F B_n L_s} \tag{56}$$

where T_a denotes the accumulation time, σ^0 denotes the clutter backscattering coefficient, k denotes the Boltzmann constant, T_0 denotes the temperature, F denotes the noise factor, and L_s denotes the radar system loss. According to Table 5, the relationship between CNR and elevation angle in a missile-borne radar system is shown in Fig. 9, where the backscattering coefficient of the observed clutter is modeled by the Morchin model [60] and the observed scene belongs to the hills. It can be seen from the figure that the longer the slant range, the lower the CNR. It is because with the increase of radar surveillance distance, both the electromagnetic-wave propagation attenuation and the decreased clutter backscattering coefficient jointly lower the clutter power. Therefore, as for the main-lobe clutter components located at the near-range and middle-range, the clutter suppression is necessary in order to improve the target output signal-to-clutter-plus-noise ratio (SCNR).

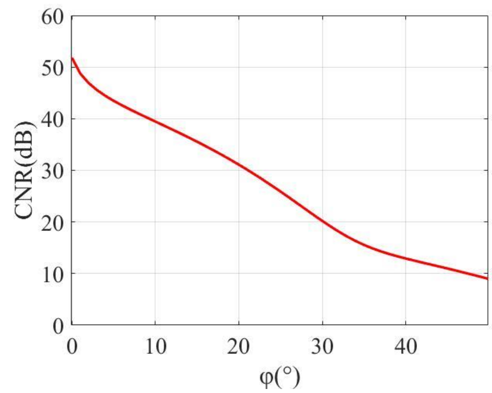

Fig. 9. Relationship between CNR and elevation angle in a side-looking missile-borne radar.

Fig. 10(a) shows the clutter distribution in the range-Doppler domain, from which it can be seen that the main-lobe clutter Doppler spectrum broadens severely due to the high-speed motion of the missile-borne platform. After performing the averaging operation along range dimension, Fig. 10(b) depicts the averaged power with the form of dB. Obviously, the clutter 3-dB main-lobe width is about 10000 Hz, which is consistent with the system parameters listed in Table 3 and Table 4. After performing the spatial channel correlation with respect to channel 1 and channel 8, the interferogram is shown in Fig. 10(c), from which it can be seen that the interferometric phase varies linearly with the Doppler frequency in the main-lobe region and changes randomly in the other side-lobe regions due to the randomly fluctuated noise influences. In addition, for the stationary clutter, the clutter space-time spectrum exhibits an ideal oblique line in this side-looking mode, as shown in Fig. 10(d), indicating that the traditional STAP methods can be applied to achieve a good clutter suppression performance in this ideal configuration.

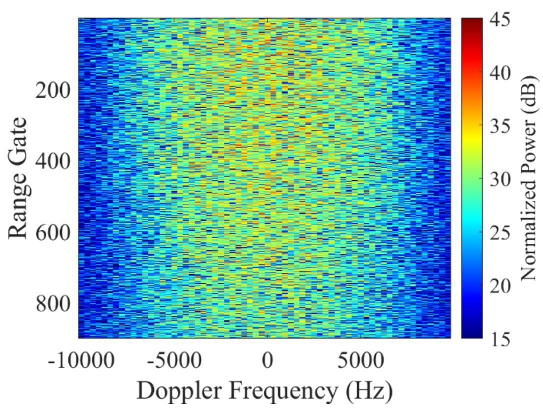

(a)

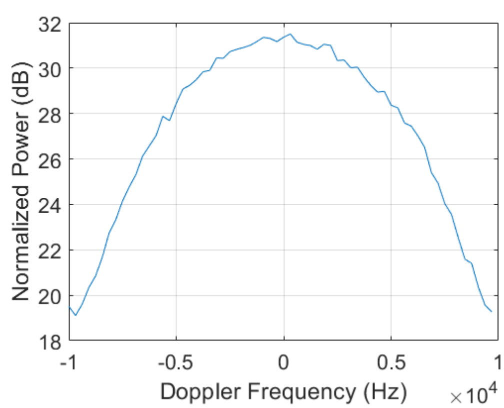

(b)

Accepted Manuscript
Version of record at: https://doi.org/10.1109/TAES.2022.3147136

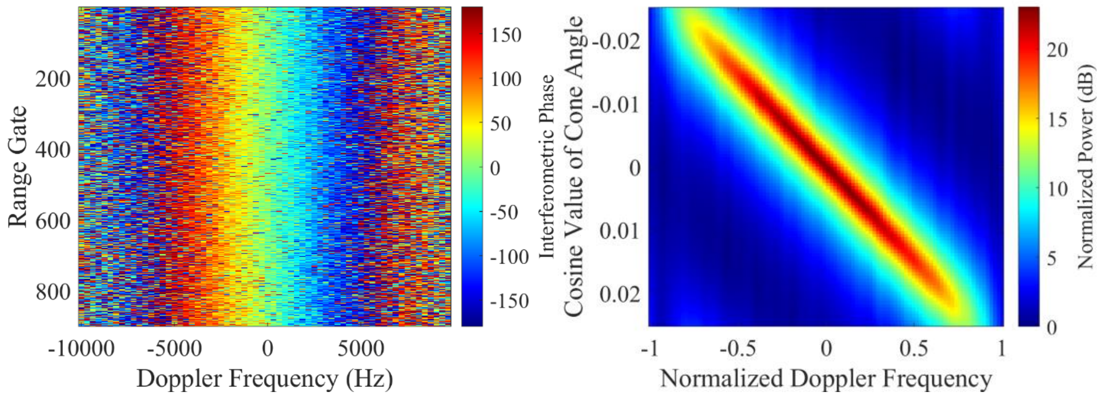

(c) (d)

Fig. 10. Processing results of ground clutter in a horizontal side-looking missile-borne radar system. (a) Clutter range-Doppler spectrum. (b) Doppler spectrum averaged from the range dimension. (c) Interferogram with respect to channel 1 and channel 8. (d) Clutter space-time spectrum distribution.

2) Horizontal Forward-looking Clutter Spectrum Analysis

The range-Doppler spectrum and space-time spectrum of the ground clutter in a horizontal forward-looking missile-borne radar system are shown in Fig. 11. From Fig. 11(a), it can be observed that the clutter Doppler center is obviously curved in different range units, indicating that the severe range dependence is present. Fig. 11(b) depicts the clutter space-time spectrum. As it is apparent, different from the space-time spectrum in a side-looking mode (see Fig. 10(d)), the space-time spectrums of clutter components located at the different range cells are not coincident due to the clutter range dependence in a forward-looking configuration. In addition, it can be also observed from Fig. 11(b) that the clutter space-time spectrum shows a transverse band rather than the ellipse trajectory. It is because: 1) the clutter components in each range gate are mainly concentrated on the zero-frequency regions in the horizontal forward-looking configuration (the repetitive distribution phenomenon of clutter ridge in the angle-Doppler domain is theoretically discussed in Appendix E) and 2) the space-time spectrum in Fig. 11(b) is the superimposing result of a large number of ellipse-shaped space-time spectrums with respect to different range positions. As a result, in order to improve the subsequent clutter cancellation performance, the effective clutter spectrum compensation becomes necessary.

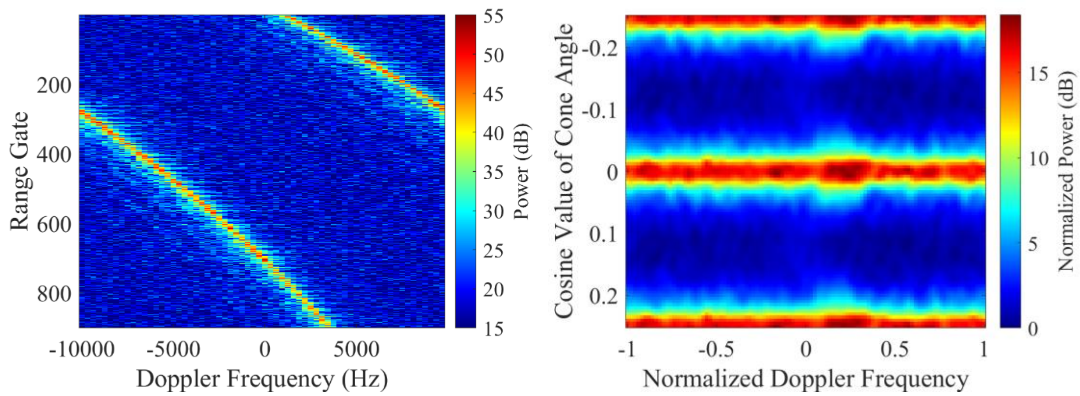

(a) (b)

Fig. 11. Processing results of ground clutter in a horizontal forward-looking missile-borne radar system. (a) Clutter range-Doppler spectrum. (b) Clutter space-time spectrum.

3) Diving Forward-looking Clutter Spectrum Analysis

Table 6 Angle Parameters

Elevation angle of beam center	60°
Diving angle	15°/30°/45°
Spinning angular velocity	360°/s
Coning angular velocity	180°/s
Initial spinning angle	15°/30°/45°
Intersection angle	15°/30°
Initial coning angle	30°/45°/60°

The missile-borne platform will inevitably perform the diving motion when implementing the moving target attacking. In the meantime, the missile platform will perform the spinning and coning motions in order to eliminate the thrust misalignment influence. In the following, the clutter spatial-temporal characteristics in a diving forward-looking configuration with the considerations of complex spinning and coning motions are analyzed. The angle parameters in this simulation are listed in Table 6.

In the following, we firstly analyze the influence of diving angle, where the spinning angle and the coning angle are both set as 0°. Fig. 12 shows the processing results with the diving angle being set as 15°, 30°, and 45°. From the figures, it can be seen that the clutter non-stationarity is significantly influenced by the diving angle. In addition, when the diving angle is the complementary angle of the beam center elevation angle, the clutter non-stationarity is relatively low, as clarified in Appendix A.

Accepted Manuscript
Version of record at: https://doi.org/10.1109/TAES.2022.3147136

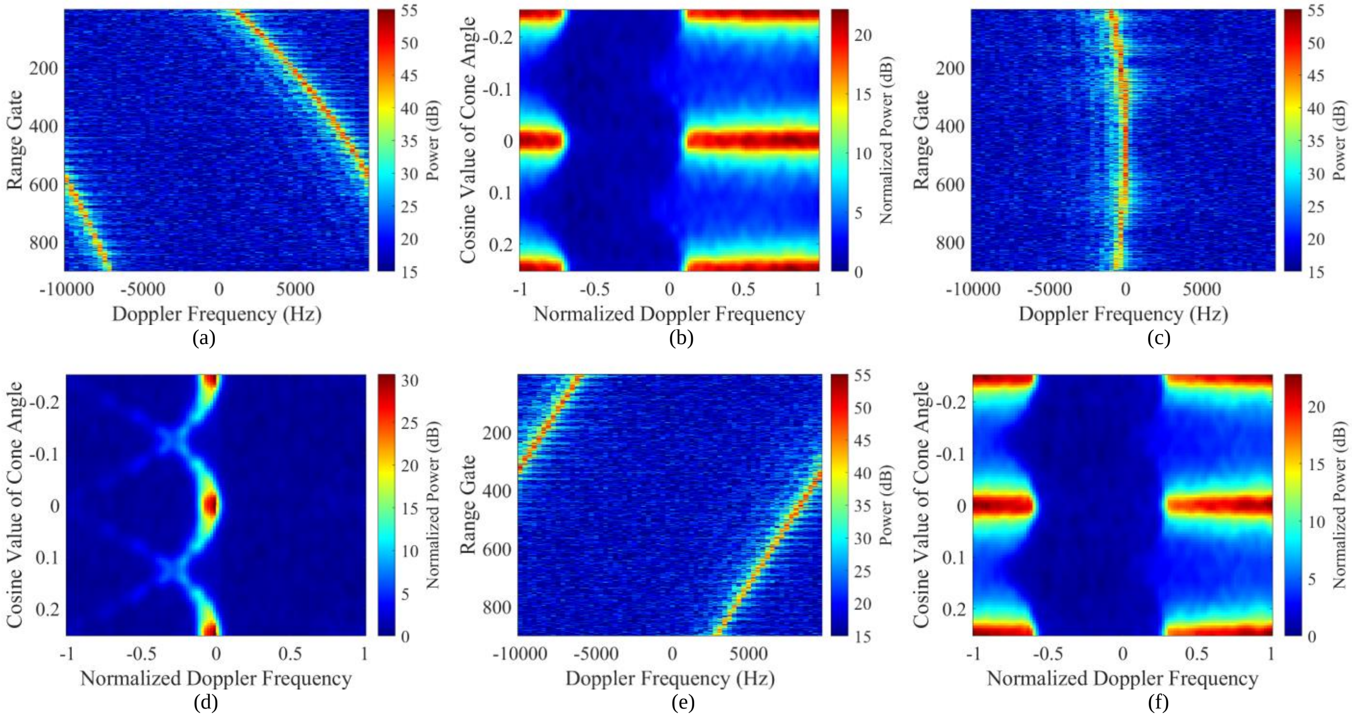

Fig. 12. Processing results with different diving angles. (a) Clutter range-Doppler spectrum with a diving angle of 15 °. (b) Clutter space-time spectrum with a diving angle of 15 °. (c) Clutter range-Doppler spectrum with a diving angle of 30 °. (d) Clutter space-time spectrum with a diving angle of 30 °. (e) Clutter range-Doppler spectrum with a diving angle of 45 °. (f) Clutter space-time spectrum with a diving angle of 45 °.

In the following, the influence of spinning motion is analyzed, where the diving angle is set as 15 ° and the coning angle is set as 0 °. The processing results with the spinning angle being set as 15 °, 30 °, and 45 ° are, respectively, shown in Fig. 13(a)~(f). From the range-Doppler spectrums, it can be seen that the clutter spectrum slightly broadens with the increase of spinning angle. In addition, it can be seen from Fig. 13(b), (d), and (f) that in the case of different spinning angles, clutter spatial center frequencies are different due to the platform spinning motion. Therefore, the 2-D angle-Doppler compensation is necessary in a spinning diving forward-looking configuration.

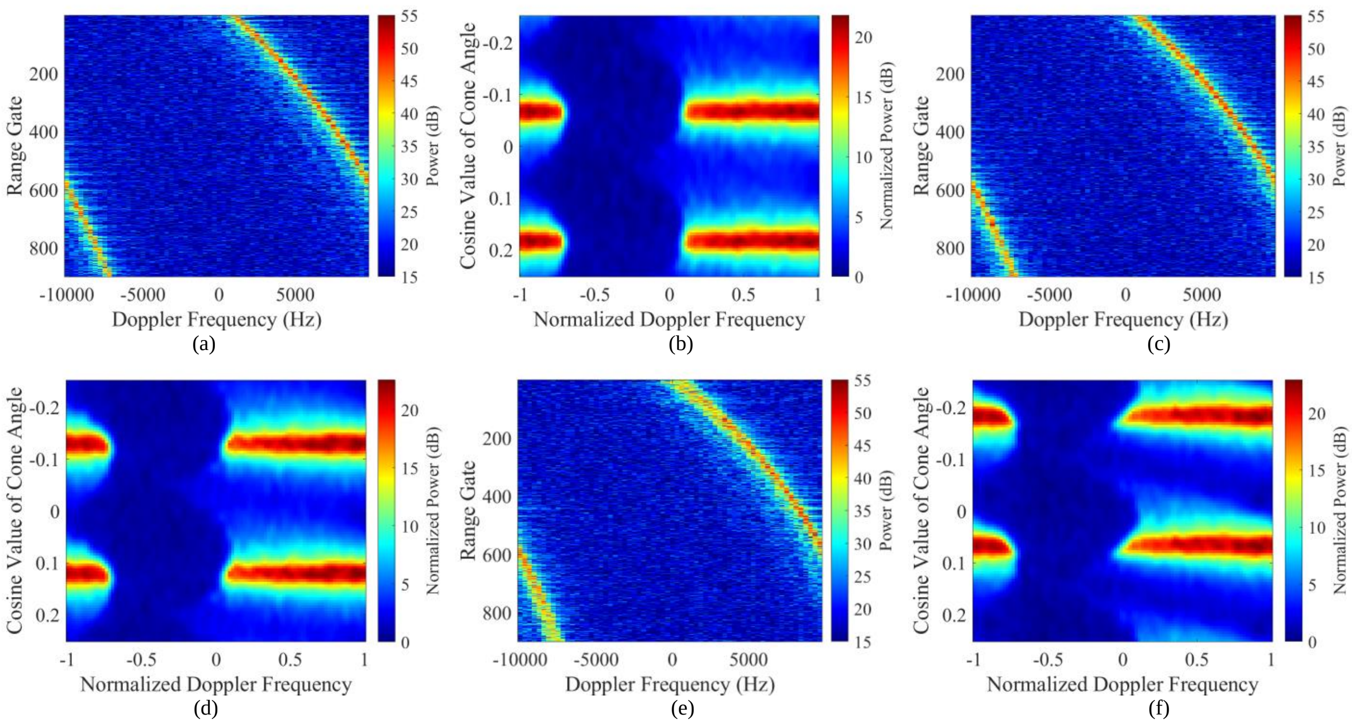

Fig. 13. Processing results with different spinning angles. (a) Clutter range-Doppler spectrum with a spinning angle of 15 °. (b) Clutter space-time spectrum with a spinning angle of 15 °. (c) Clutter range-Doppler spectrum with a spinning angle of 30 °. (d) Clutter space-time spectrum with a spinning angle of 30 °. (e) Clutter range-Doppler spectrum with a spinning angle of 45 °. (f) Clutter space-time spectrum with a spinning angle of 45 °.

Accepted Manuscript
Version of record at: https://doi.org/10.1109/TAES.2022.3147136

In the following, the influence of coning motion is analyzed, where the diving angle is 15 °and the spinning angle is 15 °. The processing results with different coning angles and intersection angles are shown in Fig. 14. It can be observed from the figures that the platform conical rotation will also cause the slightly broadening of Doppler spectrum and the range dependence of spatial frequency. In addition, as the intersection angle changes, the Doppler spectrum shifts.

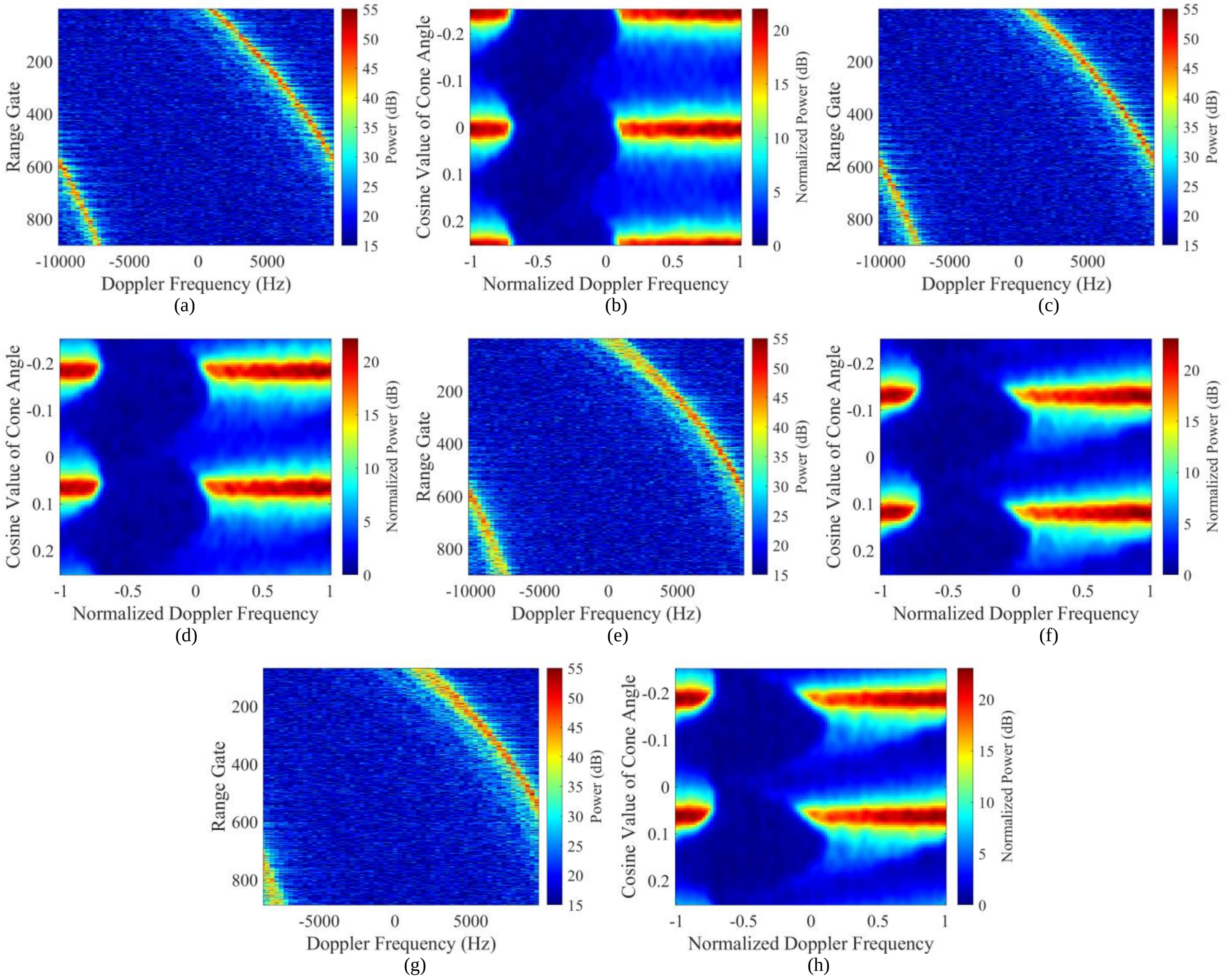

Fig. 14. Processing results with different coning angles and intersection angles. (a) Clutter range-Doppler spectrum with an intersection angle of 15 °and a coning angle of 30 °. (b) Clutter space-time spectrum with an intersection angle of 15 °and a coning angle of 30 °. (c) Clutter range-Doppler spectrum with an intersection angle of 15 °and a coning angle of 45 °. (d) Clutter space-time spectrum with an intersection angle of 15 °and a coning angle of 45 °. (e) Clutter range-Doppler spectrum with an intersection angle of 15 °and a coning angle of 60 °. (f) Clutter space-time spectrum with an intersection angle of 15 °and a coning angle of 60 °. (g) Clutter range-Doppler spectrum with an intersection angle of 30 °and a coning angle of 60 °. (h) Clutter space-time spectrum with an intersection angle of 30 °and a coning angle of 60 °.

B. Clutter Suppression Performance Analysis

Table 7 Angle Parameters

Elevation angle of beam center	60 °
Diving angle	20 °
Spinning angular velocity	360 °/s
Coning angular velocity	180 °/s
Initial spinning angle	60 °
Intersection angle	20 °
Initial coning angle	75 °

Fig. 15(a)~(b) show the clutter spectrums in a diving forward-looking missile-borne radar system before the compensation processing (the system parameters refer to Table 3~5 and Table 7), from which it can be observed that the severe range dependence will interfere the subsequent clutter suppression procedure. After performing the 2-D angle-Doppler compensation, the processing results are shown in Fig. 15(c)~(d), from which it can be seen that the Doppler center frequencies in different range gates are the same and the clutter ridge in the angle-Doppler domain exhibits an ideal ellipse trajectory.

After applying the FA method [13], [14], the SP method, and the proposed TSWSP ($K_m = 3$) method, Fig. 15(e)~(h) show the clutter rejection results. From the figures, it can be observed that the proposed TSWSP method exhibits a better clutter suppression performance than those of the FA and SP methods. It is because: 1) the proposed TSWSP method can utilize more auxiliary channel data via the temporal sliding window processing to perform the subsequent spatially filtering, thus

Accepted Manuscript
Version of record at: https://doi.org/10.1109/TAES.2022.3147136

significantly improving the clutter suppression robustness; and 2) the proposed method can effectively mitigate the effect of spectrum leakage in comparison with the FA and SP methods.

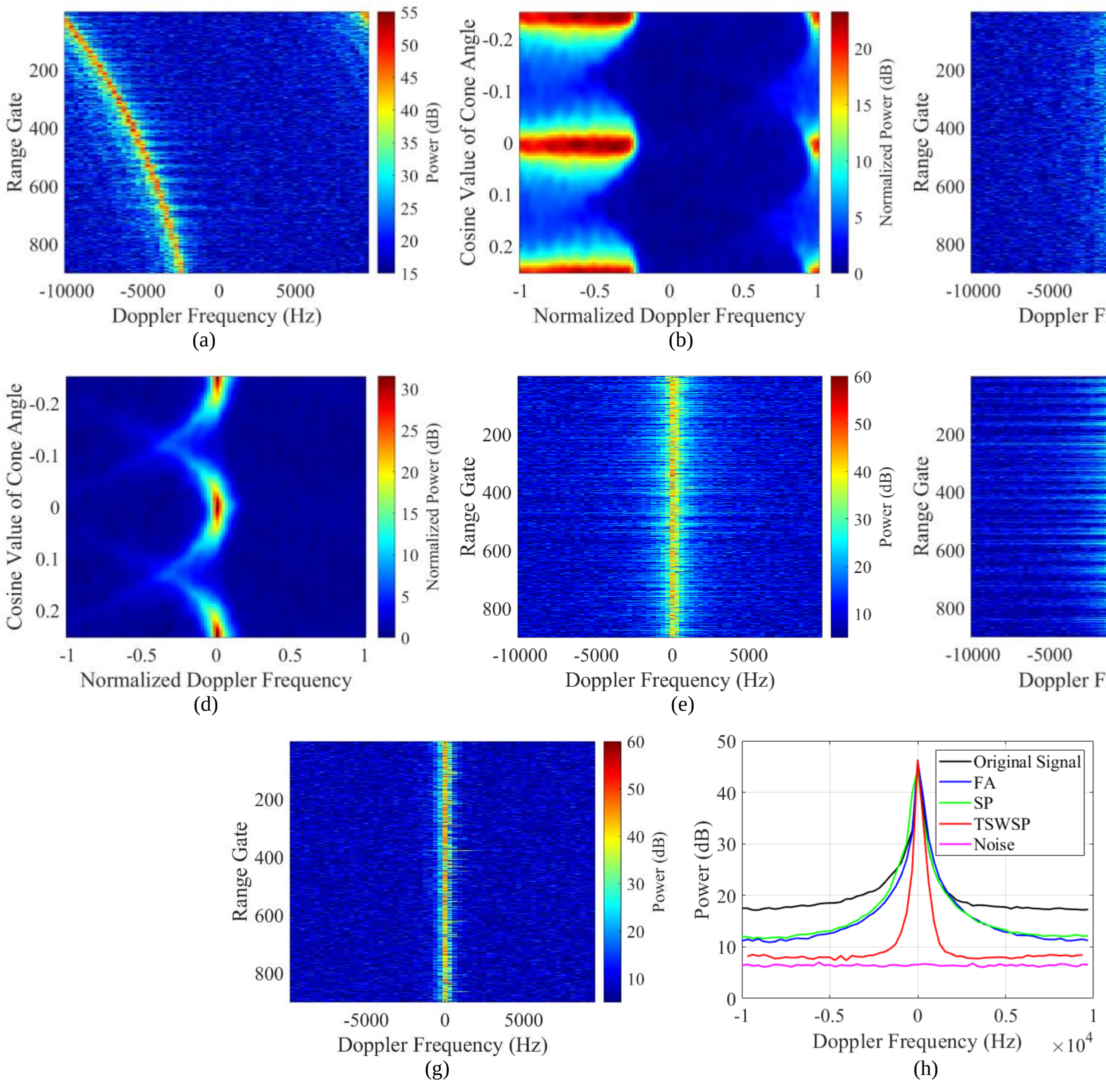

Fig. 15. Clutter suppression processing results. (a) Clutter range-Doppler spectrum before spectrum compensation. (b) Clutter space-time spectrum before spectrum compensation. (c) Clutter range-Doppler spectrum after performing the 2-D angle-Doppler compensation. (d) Clutter space-time spectrum after performing the 2-D angle-Doppler compensation processing. (e) Clutter suppression result by using the FA method. (f) Clutter suppression result by using the SP method. (g) Clutter suppression result by using the TSWSP method. (h) Averaged Doppler spectrum after clutter cancellation by applying the FA, SP, and TSWSP methods.

Based on the clutter simulation results in Fig. 15, a moving target with different radial velocities is added in the clutter and noise background, with the final SCNR loss in dB provided in Fig. 16. Obviously, compared with the FA and SP methods, the proposed TSWSP method possesses the better target detection ability.

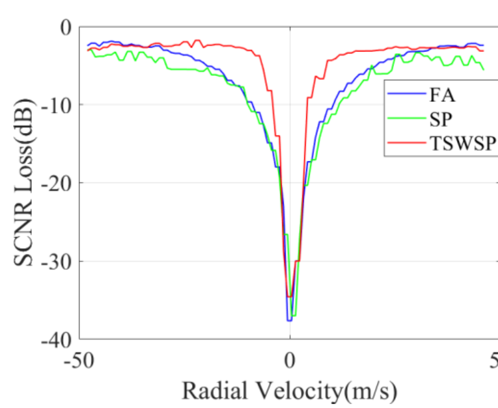

Fig. 16. SCNR loss curves.

In the following, the influences of different numbers of training samples and spatial channels on the FA, SP, and TSWSP methods are considered, with the simulated results

Accepted Manuscript
Version of record at: https://doi.org/10.1109/TAES.2022.3147136

listed in Table 8 and shown in Fig. 17, where the radial velocity of a moving target is set as 15m/s and the false alarm probability is set as 10^{-6}. It can be observed from the table and figures that the target SCNR loss and detection probability P_d improve with the increase of training samples and spatial channels by using the FA method. But for the SP and TSWSP algorithms, SCNR loss and detection probability remain a stable level with the increase of training samples because the clutter covariance matrix reconstruction procedure is avoided. In addition, with the adoption of more spatial channels, the performances of SCNR loss and detection probability by using these methods become more ameliorative, as shown in Fig. 17, where the TSWSP exhibits the higher detection probability.

Table 8

range units		500	550	600	650	700	750	800
SCNR loss	FA	-7.25	-7.19	-7.13	-7.07	-6.97	-6.94	-6.82
	SP	-6.94	-7.07	-7.09	-7.18	-7.11	-7.06	-7.10
	TSWSP	-3.17	-3.15	-3.07	-3.12	-3.15	-3.26	-3.23
P_d	FA	0.111	0.116	0.121	0.127	0.137	0.139	0.152
	SP	0.139	0.127	0.125	0.117	0.124	0.128	0.125
	TSWSP	0.859	0.863	0.875	0.867	0.862	0.845	0.849

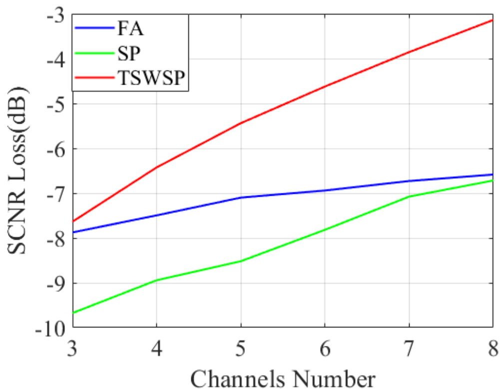

(a)

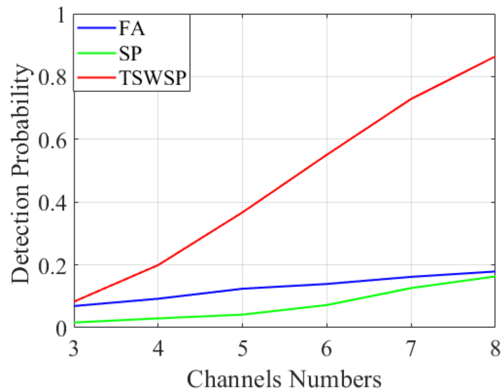

(b)

Fig. 17. SCNR loss and detection probability versus spatial channel number. (a) SCNR loss versus different spatial channels by using the FA, SP, and TSWSP methods. (b) Detection probability versus different spatial channels by using the FA, SP, and TSWSP methods.

C. Real-Measured Airborne Data Analysis

Considering that it is difficult to obtain the real-measured missile-borne radar data, the real-measured multi-channel airborne radar data is substituted to comparatively analyze the clutter suppression performances of the FA, SP, and TSWSP methods. The system parameters of this airborne radar with the side-looking observation configuration are listed in Table 9.

Table 9 Multi-channel airborne radars system parameters

Carrier frequency	2.3 GHz
Pulse repetition frequency	2000 Hz
Number of received channels	5
Number of pulses in a CPI	100

The range-Doppler spectrum and the space-time spectrum of this real-measured clutter are shown in Fig. 18. Apparently, due to the platform motion, the clutter spectrum broadens severely, causing the difficulty of slow-moving target detection. Therefore, the effective clutter suppression method is required. In addition, the clutter space-time spectrum in Fig. 18(b) exhibits an ideal oblique trajectory, indicating that the range dependence can be ignored for this real-measured airborne radar system.

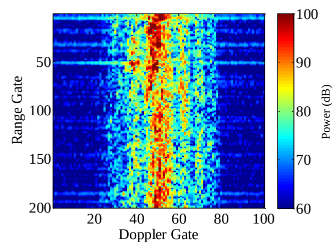

(a)

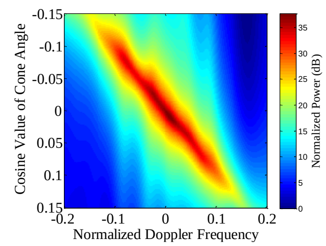

(b)

Fig. 18. Clutter range-Doppler spectrum and space-time spectrum of the real-measured airborne clutter. (a) Clutter range-Doppler spectrum. (b) Clutter space-time spectrum.

The range-Doppler spectrums and the 1-D Doppler slice averaged from range dimension after applying the FA, SP, and TSWSP (K_m=3, K_m=5) methods are shown in Fig. 19, from which it can be seen that the TSWSP has better clutter suppression performance than those of the FA and SP methods in the side-lobe region, as discussed in Section III-B. In addition, compared to the TSWSP method with $K_m = 3$, the TSWSP method with $K_m = 5$ shows slight performance improvement, but leads to higher computational complexity in the meantime. Therefore, the TSWSP method with $K_m = 3$ is more suitable to perform the clutter suppression in practical engineering applications.

Accepted Manuscript
Version of record at: https://doi.org/10.1109/TAES.2022.3147136

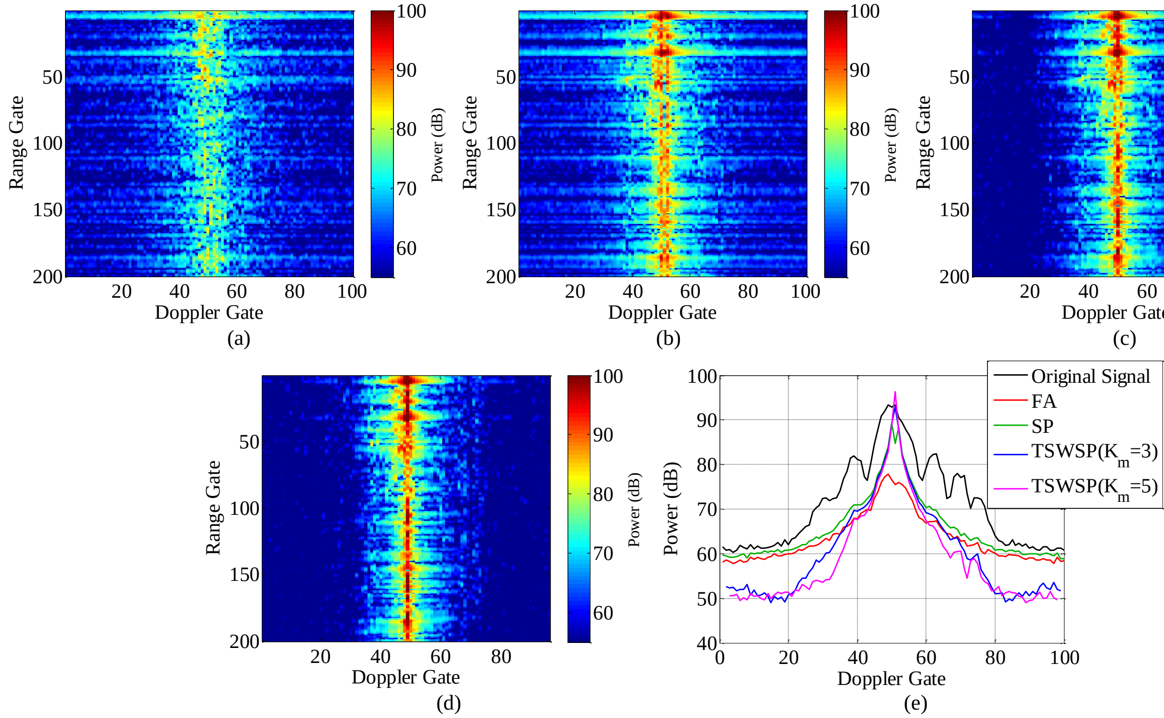

Fig. 19. Clutter range-Doppler spectrums and 1-D Doppler slice averaged from range direction after applying the FA, SP, and TSWSP methods. (a) Clutter range-Doppler spectrum by using the FA method. (b) Clutter range-Doppler spectrum by using the SP method. (c) Clutter range-Doppler spectrum by using the TSWSP method with $K_m = 3$. (d) Clutter range-Doppler spectrum by using the TSWSP method with $K_m = 5$. (e) 1-D Doppler slice averaged from range dimension by applying the FA, SP, and TSWSP methods.

V. Conclusions

The moving target detection and precise striking abilities of a missile-borne radar system play an important role in a modern battlefield. This paper focuses on the researches of missile-borne radar clutter modeling, clutter non-stationary compensation, and robust clutter suppression in a multi-channel array configuration with the consideration of complex motions including diving, spinning, and coning. The main contributions of this paper can be summarized as follows:

1) Accurate multi-channel slant-range models of ground clutter in different working situations are given, including the side-looking case, the forward-looking case, the forward-looking case with the diving flight, and the forward-looking case with the joint diving, spinning, and coning motions.

2) An adaptive angle-Doppler compensation algorithm based on IAA, autocorrelation processing, and GLS is proposed to compensate the spectrum centers along spatial angular frequency direction and Doppler frequency direction, thus providing more effective i.i.d. samples for the subsequent multi-channel clutter cancellation.

3) A robust clutter rejection method, i.e., TSWSP, is proposed, which creates more sets of radar echo data via the time-domain sliding window processing. Then the data vectors are grouped together in the space-domain, which is equivalent to increasing the spatial degree of freedom of a missile-borne radar system, effectively improving the clutter suppression robustness.

Therefore, the precise missile-borne radar clutter modeling, simulation, space-time spectrum analysis, 2-D spectrum compensation, and robust clutter rejection are developed. The effectiveness and feasibility of the proposed method have been validated by both simulation experiments and real-measured data processing results. How to precisely build the multi-channel signal model of the complex sea clutter scene with complex randomly internal motions in a missile-borne radar system and develop the robust sea clutter suppression technique will be under our future investigation.

APPENDIX A

In this Appendix, we will analyze the clutter range-dependent properties in different diving angles. For the missile-borne radar in a forward-looking configuration with diving flight, according to (3), the clutter Doppler center frequency can be given by

$$f_a = \frac{2\left(\sin\varphi_i \cos\theta_i \cos\gamma + \cos\varphi_i \sin\gamma\right)V_{ap}}{\lambda} \tag{A1}$$

Additionally, the cosine of the spatial cone angle ψ is expressed as

$$\cos\psi = \sin\varphi_i \sin\theta_i \tag{A2}$$

Obviously, it can be seen from (A1) and (A2) that the clutter Doppler centers at different elevation angles will not be coincided, indicating that the observed clutter is range-dependent. Also, the degree of clutter range-dependence is related to the platform diving angle γ.

Consider that in a forward-looking mode, the antenna pattern gains of the main-lobe clutter components located in front of phased array panel, i.e., the angle regions with the azimuth angles around 0°, are relatively high (also see the antenna

Accepted Manuscript
Version of record at: https://doi.org/10.1109/TAES.2022.3147136

pattern simulation results in Fig. 7). Then, the clutter center frequency in the case of $\theta_i = 0$ is rewritten as

$$f_{a0} = \frac{2\left(\sin\varphi_i \cos\gamma + \cos\varphi_i \sin\gamma\right)V_{ap}}{\lambda} \tag{A2}$$

The derivative of f_{a0} with respect to the elevation angle is noted as

$$\frac{\partial f_{a0}}{\partial \varphi_i} = \frac{2\cos\left(\varphi_i + \gamma\right)V_{ap}}{\lambda} \tag{A4}$$

Therefore, when the elevation angle φ_i is complementary to the diving angle γ, the change rate of Doppler center frequency is relatively small, which means that the clutter range-dependent degree is relatively small, i.e., the clutter spatial vectors corresponding to different elevation angles approximately coincide.

In the following, some simulation examples are provided to validate the above theoretical analysis. In this simulation, the carrier frequency is 30 GHz, the platform velocity is 1700 m/s, and the angles of γ and φ_i in three cases are listed in Table 10, respectively.

Table 10

	γ		The values of φ_i		
Case 1	30 °	1st group	25 °	30 °	35 °
Case 2	45 °	2nd group	40 °	45 °	50 °
Case 3	60 °	3rd group	55 °	60 °	65 °

Fig. 20, Fig. 21, and Fig. 22 show, respectively, the theoretical analysis results of clutter angle-Doppler spectrums in the case of $\gamma = 30°$, $\gamma = 45°$, and $\gamma = 60°$. From the figures, one can clearly see that when the elevation angle φ_i is complementary to the diving angle γ, the clutter range dependence is smallest (the spatial cone angle differences of clutter components in different elevation angles are smallest in this case, which means that the clutter components in different ranges exhibit the closest spatial vectors), demonstrating the correction of the clutter range-Doppler distributions in Fig. 12(c) and (d).

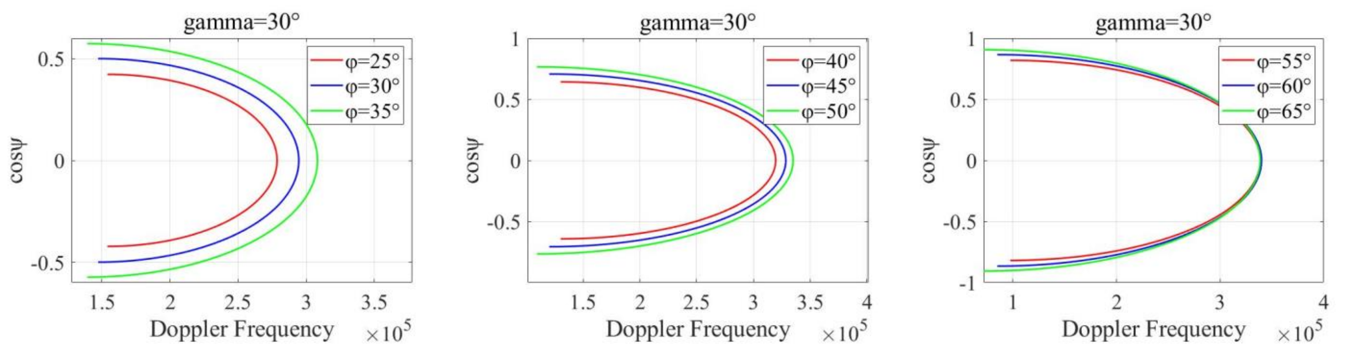

(a) (b) (c)

Fig. 20. Clutter angle-Doppler spectrum in the case of $\gamma = 30°$. (a) Angle-Doppler spectrum in the case of $\gamma = 30°$ with elevation angle $\varphi_i = 25°$, $\varphi_i = 30°$, and $\varphi_i = 35°$. (b) Angle-Doppler spectrum in the case of $\gamma = 30°$ with elevation angle $\varphi_i = 40°$, $\varphi_i = 45°$, and $\varphi_i = 50°$. (c) Angle-Doppler spectrum in the case of $\gamma = 30°$ with elevation angle $\varphi_i = 55°$, $\varphi_i = 60°$, and $\varphi_i = 65°$.

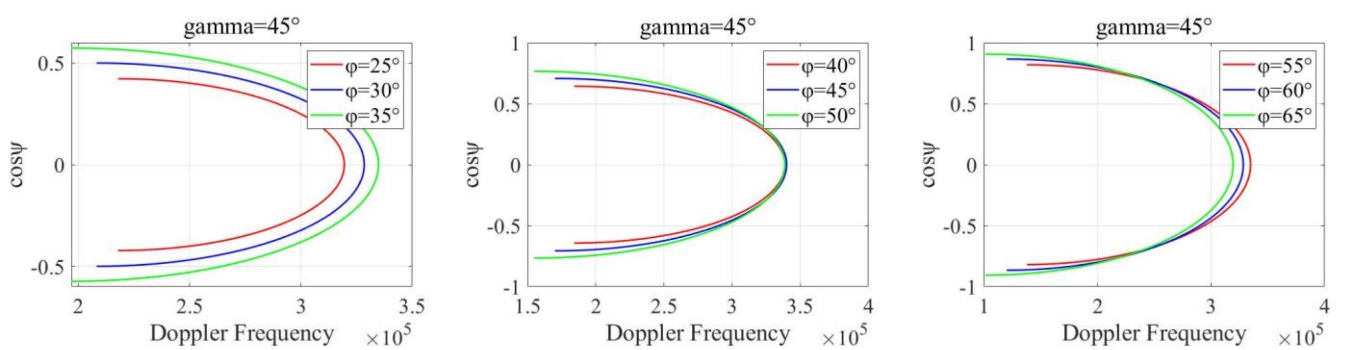

(a) (b) (c)

Fig. 21. Clutter angle-Doppler spectrum in the case of $\gamma = 45°$. (a) Angle-Doppler spectrum in the case of $\gamma = 45°$ with elevation angle $\varphi_i = 25°$, $\varphi_i = 30°$, and $\varphi_i = 35°$. (b) Angle-Doppler spectrum in the case of $\gamma = 45°$ with elevation angle $\varphi_i = 40°$, $\varphi_i = 45°$, and $\varphi_i = 50°$. (c) Angle-Doppler spectrum in the case of $\gamma = 45°$ with elevation angle $\varphi_i = 55°$, $\varphi_i = 60°$, and $\varphi_i = 65°$.

Accepted Manuscript
Version of record at: https://doi.org/10.1109/TAES.2022.3147136

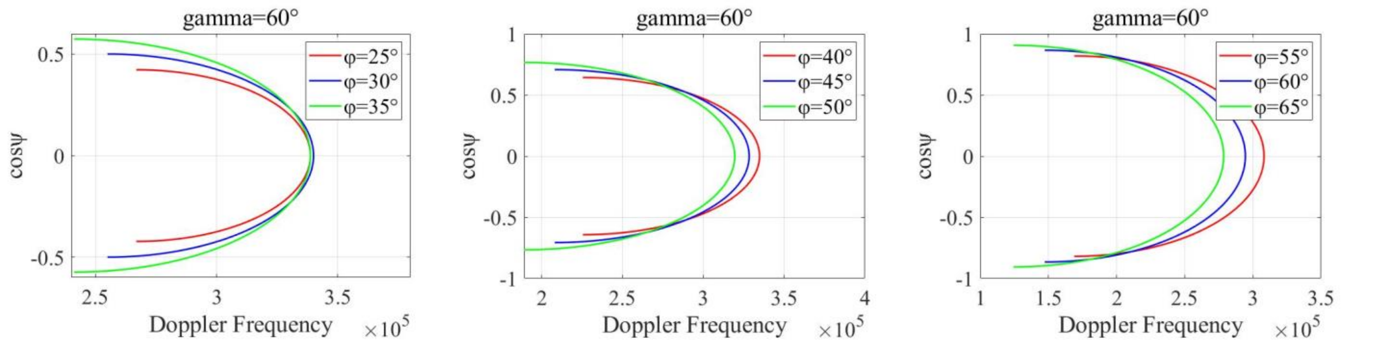

(a) (b) (c)

Fig. 22. Clutter angle-Doppler spectrum in the case of $\gamma=60°$. (a) Angle-Doppler spectrum in the case of $\gamma=60°$ with elevation angle $\varphi_i=25°$, $\varphi_i=30°$, and $\varphi_i=35°$. (b) Angle-Doppler spectrum in the case of $\gamma=60°$ with elevation angle $\varphi_i=40°$, $\varphi_i=45°$, and $\varphi_i=50°$. (c) Angle-Doppler spectrum in the case of $\gamma=60°$ with elevation angle $\varphi_i=55°$, $\varphi_i=60°$, and $\varphi_i=65°$.

APPENDIX B

In order to calculated the 3-D coordinate values of P_i^{land} in O_{prec}-$x_{prec}y_{prec}z_{prec}$ coordinate system, the coordinate origin O should be shifted into the origin O_{prec}, and thus the coordinate position calculation of O_{prec} in O-xyz coordinate becomes necessary.

Assume that the 3-D coordinate relationship is projected into the 2-D plane yOz from x-axis, with the projection relationship of spatial positions provided in Fig. 23, where the dotted circle denotes the coning motion plane perpendicular to $\overline{O_{prec}A}$ axis.

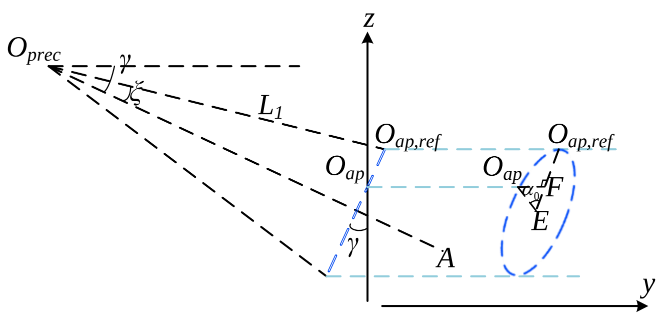

Fig. 23. The projecting relationship from the 3-D spatial coordinate (see Fig. 5) into the 2-D plane yOz from x-axis.

Assume that the antenna panel rotates at an angle of α_0 around the translational velocity axis, i.e., $\overline{O_{prec}A}$, then the reference point $O_{ap,prec}$ is shifted from the highest point $O_{ap,ref}$ to the point O_{ap}, as shown in Fig. 23, from which the x-axis coordinate of the point O_{prec} in O-xyz coordinate system can be calculated as

$$-\left|\overline{O_{ap}F}\right| = -L_1 \sin\xi \sin\alpha_0 \tag{B1}$$

From Fig. 23, it can observed that the height difference between O_{prec} and $O_{ap,ref}$ is $L_1\sin(\gamma-\xi)$, and the height difference between O_{ap} and the reference point $O_{ap,ref}$ is $\left|\overline{O_{ap,ref}F}\right|\cos\gamma = L_1\sin\xi(1-\cos\alpha_0)\cos\gamma$. Assume that the z-axis coordinate of the antenna panel center O_{ap} is H at this moment, then the coordinate of O_{prec} along z-axis can be expressed as

$$H + L_1\sin\xi\cos\gamma(1-\cos\alpha_0) + L_1\sin(\gamma-\xi) \tag{B2}$$

In addition, the distance difference with respect to O_{ap} and $O_{ap,ref}$ along y-axis can be calculated as $\left|\overline{O_{ap,ref}F}\right|\sin\gamma = L_1\sin\xi(1-\cos\alpha_0)\sin\gamma$, and the distance between $O_{ap,ref}$ and O_{prec} is $L_1\cos(\gamma-\xi)$. Then, the y-axis coordinate of O_{prec} is noted as

$$-L_1\cos(\gamma-\xi) + L_1\sin\xi\sin\gamma(1-\cos\alpha_0) \tag{B3}$$

Therefore, based on the 3-D coordinate values of O_{prec} in O-xyz coordinate system, after performing the coordinate translation, the 3-D coordinate values of the ground scatterer P_i^{land} in $O_{prec}-x_{prec}y_{prec}z_{prec}$ coordinate can be given by

$$\begin{pmatrix} x_1 \\ y_1 \\ z_1 \end{pmatrix} = \begin{pmatrix} x_{P_i^{land}} \\ y_{P_i^{land}} \\ z_{P_i^{land}} \end{pmatrix} - \begin{pmatrix} -L_1\sin\xi\sin\alpha_0 \\ -L_1\cos(\gamma-\xi) + L_1\sin\xi\sin\gamma(1-\cos\alpha_0) \\ H + L_1\sin\xi\cos\gamma(1-\cos\alpha_0) + L_1\sin(\gamma-\xi) \end{pmatrix} \tag{B4}$$

where $\left(x_{P_i^{land}}, y_{P_i^{land}}, z_{P_i^{land}}\right)$ refers to the 3-D coordinates of P_i^{land} in O-xyz coordinate. It can be seen from Fig. 5 that the coordinate origin has been shifted into the point O_{prec}. At this time, in order to make the y-axis coincide with the y_{prec}-axis (see Fig. 5), the obtained coordinate in Fig. 5 should clockwise rotate at an angle of $\gamma-\xi$, i.e.,

$$\begin{pmatrix} x_2 \\ y_2 \\ z_2 \end{pmatrix} = \begin{pmatrix} 1 & 0 & 0 \\ 0 & \cos(\gamma-\xi) & -\sin(\gamma-\xi) \\ 0 & \sin(\gamma-\xi) & \cos(\gamma-\xi) \end{pmatrix} \begin{pmatrix} x_1 \\ y_1 \\ z_1 \end{pmatrix} \tag{B5}$$

Obviously, the calculated coordinate in (B5) does not consider the spinning and coning motion influences, which will induce the large slant-range error if these two typical rotational motions are ignored. According to Fig. 5, assume that the antenna panel clockwise spins an angle of β_0 around $\overline{O_{prec}O_{ap}}$-$axis$, then one has

Accepted Manuscript
Version of record at: https://doi.org/10.1109/TAES.2022.3147136

$$\begin{pmatrix} x_3 \\ y_3 \\ z_3 \end{pmatrix} = \begin{pmatrix} \cos\beta_0 & 0 & \sin\beta_0 \\ 0 & 1 & 0 \\ -\sin\beta_0 & 0 & \cos\beta_0 \end{pmatrix} \begin{pmatrix} x_2 \\ y_2 \\ z_2 \end{pmatrix} \tag{B6}$$

In the following, the coning motion is considered. According to the Rodrigues' rotation formula [51], when a vector $\vec{m}$ clockwise rotates at an angle of α_0 around the unit vector $\vec{k}$, the obtained coordinate of new vector, denoted by $\vec{m}'$, can be expressed as

$$\vec{m}' = \vec{m}\cos\alpha_0 + (1-\cos\alpha_0)(\vec{k}\cdot\vec{m})\vec{k} + \vec{m}\times\vec{k}\sin\alpha_0 \tag{B7}$$

where $\vec{m}=(m_x, m_y, m_z)^T$ is the vector coordinate before rotation, $\vec{m}'=(m_x', m_y', m_z')^T$ is the vector coordinate after rotation, "T" denotes the transpose, and "$\times$" represents the outer product with respect of two vectors. According to the detailed derivation in Appendix D, the new vector $\vec{m}'$ in (B7) can be rewritten as

$$\begin{pmatrix} m_x' \\ m_y' \\ m_z' \end{pmatrix} = M_{trB} \begin{pmatrix} m_x \\ m_y \\ m_z \end{pmatrix} \tag{B8}$$

where M_{trB} denotes the transformation matrix associated with the coning motion, i.e.,

$$M_{trB} = \begin{bmatrix} k_x^2\kappa + \cos\alpha_0 & k_x k_y \kappa + k_z \sin\alpha_0 & k_x k_z \kappa - k_y \sin\alpha_0 \\ k_x k_y \kappa - k_z \sin\alpha_0 & k_y^2\kappa + \cos\alpha_0 & k_y k_z \kappa + k_x \sin\alpha_0 \\ k_x k_z \kappa + k_y \sin\alpha_0 & k_y k_z \kappa - k_x \sin\alpha_0 & k_z^2\kappa + \cos\alpha_0 \end{bmatrix} \tag{B9}$$

with $\kappa = 1-\cos\alpha_0$.

According to Fig. 5, with the consideration of spinning angle of β_0, the unit vector of the coning axis $\overline{O_{prec}A}$ can be given by

$$\overrightarrow{n_{O_{prec}A}} = \begin{pmatrix} -\sin\beta_0 \sin\xi \\ \cos\xi \\ -\cos\beta_0 \sin\xi \end{pmatrix} \tag{B10}$$

Then, according to (B9), the transformation matrix M_{trB} related to coning axis $\overline{O_{prec}A}$ and rotation angle α_0 can be rewritten in (B11) at the bottom of this page.

Therefore, according to (B6), the coordinate of this ground scatterer with the consideration of coning motion can be finally expressed as

$$\begin{pmatrix} x_{P_{i,prec}} \\ y_{P_{i,prec}} \\ z_{P_{i,prec}} \end{pmatrix} = M_{trB} \begin{pmatrix} x_3 \\ y_3 \\ z_3 \end{pmatrix} = M_{trA} \begin{pmatrix} x_1 \\ y_1 \\ z_1 \end{pmatrix} \tag{B12}$$

where matrix M_{trA} can be denoted as

$$M_{trA} = M_{trB} \begin{pmatrix} \cos\beta_0 & 0 & \sin\beta_0 \\ 0 & 1 & 0 \\ -\sin\beta_0 & 0 & \cos\beta_0 \end{pmatrix} \begin{pmatrix} 1 & 0 & 0 \\ 0 & \cos(\gamma-\xi) & -\sin(\gamma-\xi) \\ 0 & \sin(\gamma-\xi) & \cos(\gamma-\xi) \end{pmatrix} \tag{B13}$$

For the convenience of analysis, the following simplified notation is applied:

$$coor_{tran} = \begin{pmatrix} -L_1 \sin\xi \sin\alpha_0 \\ -L_1\cos(\gamma-\xi) + L_1 \sin\xi \sin\gamma (1-\cos\alpha_0) \\ H + L_1 \sin\xi\cos\gamma(1-\cos\alpha_0) + L_1\sin(\gamma-\xi) \end{pmatrix} \tag{B14}$$

Finally, the 3-D coordinate values of P_i^{land} in O_{prec}-$x_{prec}y_{prec}z_{prec}$ coordinate system can be calculated as

$$\begin{pmatrix} x_{P_{i,prec}^{land}} \\ y_{P_{i,prec}^{land}} \\ z_{P_{i,prec}^{land}} \end{pmatrix} = M_{trA} \left[\begin{pmatrix} x_{P_i^{land}} \\ y_{P_i^{land}} \\ z_{P_i^{land}} \end{pmatrix} - coor_{tran} \right] \tag{B15}$$

APPENDIX C

For the arbitrary ground scatterer P_i^{land}, the instantaneous two-way slant-range related to the nth received channel is

$$R_{n,i}^{land}(t_m) = \frac{1}{2}\left[R_T(t_m) + R_{R,n}(t_m)\right] \tag{C1}$$

where $R_T(t_m)$ and $R_{R,n}(t_m)$ denote, respectively, the transmitted and received slant-range histories. In O_{prec}-$x_{prec}y_{prec}z_{prec}$ coordinate, $R_T(t_m)$ is

$$R_T(t_m) = \sqrt{R_{T,x_{prec}}^2(t_m) + R_{T,y_{prec}}^2(t_m) + R_{T,z_{prec}}^2(t_m)} \tag{C2}$$

where $R_{T,x_{prec}}(t_m)$, $R_{T,y_{prec}}(t_m)$, and $R_{T,z_{prec}}(t_m)$ denote, respectively, the relative distances between the ground scatterer P_i^{land} and the transmitted channel center position along x_{prec}-*axis*, y_{prec}-*axis*, and z_{prec}-*axis* in O_{prec}-$x_{prec}y_{prec}z_{prec}$ coordinate. The velocity components of transmitted channel center include the translational velocity V_{ap} and the coning velocity V_p, where the direction of V_{ap} coincides with $\overline{O_{prec}A}$ and the direction of the coning velocity V_p, denoted by $\vec{n_p}$, is perpendicular to $\overline{O_{ap}E}$ and $\overline{O_{prec}A}$. It should be noted that the spinning motion will not affect the position of transmitted channel position.

Accepted Manuscript
Version of record at: https://doi.org/10.1109/TAES.2022.3147136

$$M_{trB}=\begin{bmatrix} \sin^2\beta_0\sin^2\xi\cdot\kappa+\cos\alpha_0 & -\sin\beta_0\sin\xi\cos\xi\cdot\kappa-\cos\beta_0\sin\xi\sin\alpha_0 & \sin\beta_0\cos\beta_0\sin^2\xi\cdot\kappa-\cos\xi\sin\alpha_0 \\ -\sin\beta_0\sin\xi\cos\xi\cdot\kappa+\cos\beta_0\sin\xi\sin\alpha_0 & \cos^2\xi\cdot\kappa+\cos\alpha_0 & -\cos\beta_0\sin\xi\cos\xi\cdot\kappa-\sin\beta_0\sin\xi\sin\alpha_0 \\ \sin\beta_0\cos\beta_0\sin^2\xi\cdot\kappa+\cos\xi\sin\alpha_0 & -\cos\beta_0\sin\xi\cos\xi\cdot\kappa+\sin\beta_0\sin\xi\sin\alpha_0 & \cos^2\beta_0\sin^2\xi\cdot\kappa+\cos\alpha_0 \end{bmatrix} \quad \text{(B11)}$$

The unit vector of $\overline{O_{ap}E}$ is

$$\overrightarrow{n_{O_{ap}E}}=\begin{pmatrix}-\sin\beta_0\cos\xi\\ -\sin\xi\\ -\cos\beta_0\cos\xi\end{pmatrix} \quad \text{(C3)}$$

Therefore, according to $\overrightarrow{n_{O_{ap}E}}$ and $\overrightarrow{n_{O_{prec}A}}$ (see (B10)), the unit vector of coning velocity can be calculated as

$$\overrightarrow{n_p}=\overrightarrow{n_{O_{ap}E}}\times\overrightarrow{n_{O_{prec}A}}=\begin{pmatrix}\cos\beta_0\\ 0\\ -\sin\beta_0\end{pmatrix} \quad \text{(C4)}$$

The value of coning velocity is

$$V_p=\omega_p L_1\sin\xi \quad \text{(C5)}$$

In O_{prec}-$x_{prec}y_{prec}z_{prec}$ coordinate, according to (B15), the 3-D coordinate values of the ground scatterer P_i^{land} can be given by

$$P_{i,prec}^{land}=\begin{bmatrix}x_{P_{i,prec}^{land}}\\ y_{P_{i,prec}^{land}}\\ z_{P_{i,prec}^{land}}\end{bmatrix}=M_{trA}\left[\begin{pmatrix}R_{0,i}\sin\varphi_i\sin\theta_i\\ R_{0,i}\sin\varphi_i\cos\theta_i\\ 0\end{pmatrix}-coor_{tran}\right] \quad \text{(C6)}$$

where φ_i and θ_i refer to, respectively, the elevation angle and azimuth angle of P_i^{land} in O-xyz coordinate. $R_{0,i}=\dfrac{H}{\cos\varphi_i}$ denotes the initial slant-range, which can be also expressed as

$$R_{0,i}=\left|\overrightarrow{O_{ap}P_{i,prec}^{land}}\right|=\sqrt{x_{P_{i,prec}^{land}}^2+\left(y_{P_{i,prec}^{land}}-L_1\right)^2+z_{P_{i,prec}^{land}}^2} \quad \text{(C7)}$$

where the coordinate of the point O_{ap} is $(0,L_1,0)^T$ in O_{prec}-$x_{prec}y_{prec}z_{prec}$ coordinate.

For the same reason, the received slant-range corresponding to the nth received channel is noted as

$$R_{R,n}(t_m)=\sqrt{R_{R,n,x_{prec}}^2(t_m)+R_{R,n,y_{prec}}^2(t_m)+R_{R,n,z_{prec}}^2(t_m)} \quad \text{(C8)}$$

where $R_{R,n,x_{prec}}(t_m)$, $R_{R,n,y_{prec}}(t_m)$, and $R_{R,n,z_{prec}}(t_m)$ denote, respectively, the relative distances between the ground scatterer P_i^{land} and the nth received channel position along x_{prec}-*axis*, y_{prec}-*axis*, and z_{prec}-*axis*.

Considering that the nth received channel position does not coincide with the antenna panel center, the translational velocity, spinning velocity, and coning velocity will jointly affect the received channel position at different pulse moments. According to Fig. 5, the vector $\overrightarrow{O_{prec}O_n}$ is

$$\overrightarrow{O_{prec}O_n}=(d_n,L_1,0)^T \quad \text{(C9)}$$

where O_n refers to the center position of the nth received channel.

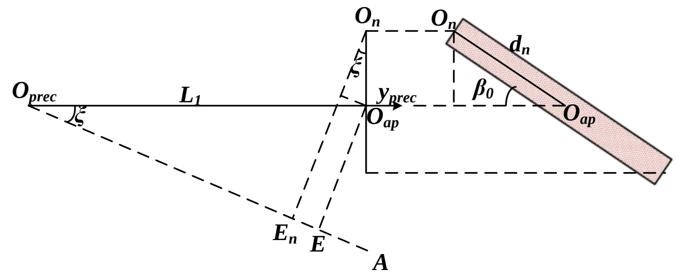

Fig. 24. The projecting relationship related to the nth received channel in the $O_{prec}O_{ap}A$ plane.

In Fig. 24, the points E_n and E are, respectively, the projection points of O_n and O_{ap} with respect to the translation velocity axis $O_{prec}A$. Clearly, the distance between the point E_n and the point E can be calculated as

$$\left|\overline{EE_n}\right|=d_n\sin\beta_0\sin\xi \quad \text{(C10)}$$

Then, the coordinate of the vector $\overrightarrow{O_{prec}E_n}$ in O_{prec}-$x_{prec}y_{prec}z_{prec}$ coordinate is obtained as

$$\overrightarrow{O_{prec}E_n}=\begin{pmatrix}-\sin\beta_0\sin\xi\\ \cos\xi\\ -\cos\beta_0\sin\xi\end{pmatrix}\left(L_1\cos\xi-d_n\sin\beta_0\sin\xi\right) \quad \text{(C11)}$$

It can be seen from (C11) that the coning radius vector with respect to O_n, denoted by $\overrightarrow{r_p}$, can be written as

$$\overrightarrow{r_p}=\overrightarrow{O_{prec}O_n}-\overrightarrow{O_{prec}E_n} \quad \text{(C12)}$$

Considering that the coning velocity of the nth received channel, denoted by $\overrightarrow{V_{pn}}$, is perpendicular to the coning radius vector $\overrightarrow{r_p}$ and the coning motion axis $\overline{O_{prec}A}$, $\overrightarrow{V_{pn}}$ can be expressed as

$$\overrightarrow{V_{pn}}=\omega_p\begin{pmatrix}L_1\sin\xi\cos\beta_0\\ -d_n\sin\xi\cos\beta_0\\ -L_1\sin\xi\sin\beta_0-d_n\cos\xi\end{pmatrix} \quad \text{(C13)}$$

Consider that x_{prec}-*axis* always coincides with the horizontal axis of antenna panel, which will not be influenced by the spinning motion; thus, the spinning velocity vector, denoted by $\overrightarrow{V_{sn}}$, will point to z_{prec}-*axis*, i.e., $\overrightarrow{V_{sn}}=(0,0,\omega_s d_n)^T$.

Then $R_T(t_m)$ and $R_{R,n}(t_m)$ can be rewritten as

$$R_T(t_m)=\left\|\overrightarrow{O_{ap}P_{i,prec}^{land}}-\overrightarrow{V_{ap}}t_m-\overrightarrow{V_p}t_m\right\| \quad \text{(C14)}$$

$$R_{R,n}(t_m)=\left\|\overrightarrow{O_nP_{i,prec}^{land}}-\overrightarrow{V_{ap}}t_m-\overrightarrow{V_{pn}}t_m-\overrightarrow{V_s}t_m\right\| \quad \text{(C15)}$$

Then (C1) can be calculated as follows:

Accepted Manuscript
Version of record at: https://doi.org/10.1109/TAES.2022.3147136

$$
\begin{aligned}
&R_{n,i}^{land}\left(t_m\right)\\
&\approx \frac{1}{2}\left\{R_{0,i}\left[1+\left(\overrightarrow{V_{ap}}+\overrightarrow{V_p}\right)^2 t_m^2 \Big/ \left(2R_{0,i}^2\right)-\overrightarrow{O_{ap}P_{i,prec}^{land}}\left(\overrightarrow{V_{ap}}+\overrightarrow{V_p}\right)t_m \Big/ R_{0,i}^2\right]\right.\\
&\qquad \left.+R_{0,i}\left[\begin{array}{l}1+\dfrac{d_n^2-2x_{P_{i,prec}^{land}}d_n}{2R_{0,i}^2}+\dfrac{\left(\overrightarrow{V_{ap}}+\overrightarrow{V_{pn}}+\overrightarrow{V_s}\right)^2 t_m^2}{2R_{0,i}^2}\\ \qquad -\overrightarrow{O_nP_{i,prec}^{land}}\left(\overrightarrow{V_{ap}}+\overrightarrow{V_{pn}}+\overrightarrow{V_s}\right)t_m \Big/ R_{0,i}^2\end{array}\right]\right\}\\
&=R_{0,i}+\frac{\widetilde{X}}{2R_{0,i}}t_m+\frac{\widetilde{Y}}{4R_{0,i}}t_m^2+\frac{d_n^2-2x_{P_{i,prec}^{land}}d_n}{4R_{0,i}}
\end{aligned} \tag{C16}
$$

where

$$
X=-\overrightarrow{O_{ap}P_{i,prec}^{land}}\left(\overrightarrow{V_{ap}}+\overrightarrow{V_p}\right)-\overrightarrow{O_nP_{i,prec}^{land}}\left(\overrightarrow{V_{ap}}+\overrightarrow{V_{pn}}+\overrightarrow{V_s}\right) \tag{C17}
$$

$$
Y=\left(\overrightarrow{V_{ap}}+\overrightarrow{V_p}\right)^2+\left(\overrightarrow{V_{ap}}+\overrightarrow{V_{pn}}+\overrightarrow{V_s}\right)^2 \tag{C18}
$$

The result in (C16) is the same as that provided in (8).

APPENDIX D

When a vector $\vec{m}$ rotates α_0 clockwise about a fixed unit vector $\vec{k}$, the resulting vector $\overrightarrow{m'}$ can be expressed as follows according to Rodriguez's rotation formula [51]:

$$
\vec{m}'=\vec{m}\cos\alpha_0+\left(1-\cos\alpha_0\right)(\vec{k}\cdot\vec{m})\vec{k}+\vec{m}\times\vec{k}\sin\alpha_0 \tag{D1}
$$

where $\vec{m}=\left(m_x,m_y,m_z\right)^T$, $\vec{k}=\left(k_x,k_y,k_z\right)^T$, and $\overrightarrow{m'}=\left(m_x',m_y',m_z'\right)^T$. Rewrite the above equation in a matrix form as below:

$$
\begin{aligned}
\begin{pmatrix}m_x'\\ m_y'\\ m_z'\end{pmatrix}&=\cos\alpha_0\begin{pmatrix}m_x\\ m_y\\ m_z\end{pmatrix}+\left(1-\cos\alpha_0\right)\left(m_xk_x+m_yk_y+m_zk_z\right)\begin{pmatrix}k_x\\ k_y\\ k_z\end{pmatrix}\\
&\quad+\sin\alpha_0\begin{pmatrix}k_zm_y-k_ym_z\\ k_xm_z-k_zm_x\\ k_ym_x-k_xm_y\end{pmatrix}\\
&=\begin{bmatrix}k_x{}^2\kappa+\cos\alpha_0 & k_xk_y\kappa+k_z\sin\alpha_0 & k_xk_z\kappa-k_y\sin\alpha_0\\ k_xk_y\kappa-k_z\sin\alpha_0 & k_y{}^2\kappa+\cos\alpha_0 & k_yk_z\kappa+k_x\sin\alpha_0\\ k_xk_z\kappa+k_y\sin\alpha_0 & k_yk_z\kappa-k_x\sin\alpha_0 & k_z{}^2\kappa+\cos\alpha_0\end{bmatrix}\begin{pmatrix}m_x\\ m_y\\ m_z\end{pmatrix}\\
&=M_{trB}\left(m_x,m_y,m_z\right)^T
\end{aligned} \tag{D2}
$$

where M_{trB} is the rotation matrix with the expression provided in (B9) and $\kappa=1-\cos\alpha_0$.

APPENDIX E

The clutter spatial steering vector can be expressed as

$$
s_s\left(\psi\right)=\exp\left(\frac{j2\pi d\cos\psi\cdot\left[0,1,\cdots,N-1\right]^{\mathrm{T}}}{\lambda}\right) \tag{E1}
$$

where ψ denotes the spatial cone angle.

Suppose that the spacing of antenna array element is half of the wavelength, and one subarray contains N_e number of antenna array elements along azimuth dimension. Then $d/\lambda=N_e/2$ holds, and (E1) can be rewritten as

$$
s_s\left(\psi\right)=\exp\left(j2\pi\cdot\frac{N_e}{2}\cos\psi\cdot\left[0,1,\cdots,N-1\right]^{\mathrm{T}}\right) \tag{E2}
$$

When $\cos\psi'=\cos\psi+2n/N_e, n\in\mathbb{Z}$, the spatial steering vector in (E2) can be expressed as

$$
\begin{aligned}
s_s\left(\psi'\right)&=\exp\left(j2\pi\cdot\frac{N_e}{2}\cos\psi\cdot\left[0,1,\cdots,N-1\right]^{\mathrm{T}}\right)\\
&\quad\odot\exp\left(j2\pi\cdot n\cdot\left[0,1,\cdots,N-1\right]^{\mathrm{T}}\right)\\
&=s_s\left(\psi\right)
\end{aligned} \tag{E3}
$$

where $\odot$ denotes the Hadamard product.

According to the system parameters in Table 5, $N_e=8$ holds. Therefore, when $\cos\psi'=\cos\psi+0.25n, n\in\mathbb{Z}$, the spatial steering vector s_s is the same for ψ and ψ'. As a result, for the angles ψ and ψ' satisfying $\cos\psi'=\cos\psi+0.25n$, the space-time spectrum powers are the same, indicating the repetitive distribution phenomenon of clutter ridge in the angle-Doppler domain (see Fig. 11).

REFERENCES

[1] Fan, H., Cui, H., and Tian, G.
A review on the 70-year development of air-to-air missiles.
Aero Weaponry, **1** (2016), 3−12.

[2] Aubry, A., Maio, A. D., Carotenuto, V., and Farina, A.
Radar phase noise modeling and effects-part I: MTI filters.
IEEE Transactions on Aerospace and Electronic Systems, **52**, 2 (2016), 698−711.

[3] Nohara, T. J., Weber, P., Premji, A., and Bhattacharya, T.
Airborne ground moving target indication using non-side-looking antennas.
IEEE Radar Conference, 1998, 269−274.

[4] Xie, W., Zhao, G, Shao, Y., and Deng, G.
Ground moving target detection technique for airborne fire-control radar.
International Congress on Image Signal Processing, **3** (2013) 1588−1592.

[5] Dawidowicz, B., Kulpa, K. S., Malanowski, M., Misiurewicz, J., Samczynski, P., and Smolarczyk, M.
DPCA detection of moving targets in airborne passive radar.
IEEE Transactions on Aerospace and Electronic Systems, **48**, 2 (2012), 1347−1357.

[6] Klemm, R.
Adaptive airborne MTI: an auxiliary channel approach.
IEE Proceedings F- Communications, Radar and Signal Processing, **134**, 3 (2008), 269−276,.

[7] Klemm, R.
Real-time adaptive airborne MTI. I. Space-time processing.
In *Proceedings of International Radar Conference*, 1996, 755−760.

[8] Klemm, R.
Real-time adaptive airborne MTI. II. Space-frequency processing.
In *Proceedings of International Radar Conference*, 1996, 430−433.

[9] Brennan, L. E., and Reed, I. S.
Theory of adaptive radar.
IEEE Transactions on Aerospace and Electronic Systems, **AES-9**, 2 (1973), 237−252.

[10] Reed, I. S., Mallett, J. D., and Brennan, L. E.
Rapid convergence rate in adaptive arrays.

IEEE Transactions on Aerospace and Electronic Systems, **AES-10**, 6 (1974), 853−863.

[11] Hussain, A., Hussain, I., Mir, I., Afzal, W., Anjum, U., and Channa, B. A.
Target parameter estimation in reduced dimension STAP for airborne phased array radar.
IEEE International Multitopic Conference, 2020,1−2.

[12] Roman, J. R., Rangaswamy, M., Davis, D. W., Zhang, Q. W., Himed, B., and Michels, J. H.
Parametric adaptive matched filter for airborne radar applications.
IEEE Transactions on Aerospace and Electronic Systems, **36**, 2 (2000), 677−692.

[13] Dipietro, R, C.
Extended factored space-time processing for airborne radar system.
In *Proceedings of Asilomar Conference on Signals, Systems &Computers*, **1** (1992), 425−430.

[14] Wang, Y., Peng, Y., and Bao, Z.
Space-time adaptive processing for airborne radar with various array orientations.
IEE Proceedings -Radar, Sonar and Navigation, **144**, 6 (1997), 330−340.

[15] Brennan, L. E., Piwinski, D. J., and Staudaher, F. M.
Comparison of space-time adaptive processing approaches using experimental airborne radar data.
In *Proceedings of the IEEE National Radar Conference*, 1993, 176−181.

[16] Wang, H., and Cai, L.
On adaptive spatial-temporal processing for airborne surveillance radar systems.
IEEE Transactions on Aerospace and Electronic Systems, **30**, 3 (1994), 660−670.

[17] Wang, Y., Chen, J., Z. Bao, and Peng, Y.
Robust space-time adaptive processing for airborne radar in nonhomogeneous clutter environments.
IEEE Transactions on Aerospace and Electronic Systems, **39**, 1 (2003), 70−81.

[18] Brown, R. D., Wicks, M. C., Zhang, Y., Zhang, Q., and Wang, H.
A space-time adaptive processing approach for improved performance and affordability.
In *Proceedings of the IEEE National Radar Conference*, 1996, 321−326.

[19] Guerci, J. R., Goldstein, J. S., and Reed, I. S.
Optimal and adaptive reduced-rank STAP.
IEEE Transactions on Aerospace and Electronic Systems, **36**, 2 (2000), 647−661.

[20] Haimovich, A. M., and Ness, Y. B.
An eigenanalysis interference canceler.
IEEE Transactions on Signal Processing, **39**, 1 (1991), 76−84.

[21] Goldstein, J. S., and Reed, I. S.
Reduced rank adaptive filtering.
IEEE Transactions on Signal Processing, **45**, 2 (1997), 472−496.

[22] Goldstein, J. S., and Reed, I. S.
A multistage representation of the wiener filter based on orthogonal projections.
IEEE Transactions on Information Theory, **44**, 7 (1998), 2943−2959.

[23] Berger, S. D., and Welsh, B. M.
Selecting a reduced-rank transformation for STAP-a direct form perspective.
IEEE Transactions on Aerospace and Electronic Systems, **35**, 2 (1999), 722−729.

[24] Haimovich, A. M., and Berin, M.
Eigenanalysis-based space-time adaptive radar: Performance analysis.
IEEE Transactions on Aerospace and Electronic Systems, **33**, 4 (1997), 1170−1179.

[25] Haimovich, A. M.
The eigencanceler: a new space-time interference canceler.
In *Proceedings of the IEEE National Radar Conference*, 1994, 194−199.

[26] Haimovich, A. M., Shah, A., and Wu, X.
Reduced-rank array processing for wireless communications with applications to IS-54/IS-136.
IEEE Transactions on Communications, **48**, 5 (2000), 743−747.

[27] Goldstein J. S., and Reed, I. S.
Subspace selection for partially adaptive sensor array processing.
IEEE Transactions on Aerospace and Electronic Systems, **33**, 2 (1997), 539−544.

[28] Friedlander, B.
A subspace method for space time adaptive processing.
IEEE Transactions on Signal Processing, **53**, 1 (2005), 74−82.

[29] Wang, Z., Xie, W., Duan, K., Gao, F., and Wang, Y.
Short-range clutter suppression based on subspace projection preprocessing for airborne radar.
In *Proceedings of the International Conference on Radar (RADAR)*, 2016, 1−4.

[30] Persico, A. R., Clemente, C., Gaglione, D., Ilioudis, C. V., Cao, J., Pallotta, L., De M. A., Proudler, I., and Soraghan, J. J.
On model, algorithms, and experiment for micro-doppler-based recognition of ballistic targets.
IEEE Transactions on Aerospace and Electronic Systems, **53**, 3 (2017), 1088−1108.

[31] Gao, H., Xie, L., Wen, S., and Kuang, Y.
Micro-doppler signature extraction from ballistic target with micro-motions.
IEEE Transactions on Aerospace and Electronic Systems, **46**, 4 (2010), 1969−1982.

[32] Sun, H., Oh, B. -S., Guo, X., and Lin, Z.
Improving the doppler resolution of ground-based surveillance radar for drone detection.
IEEE Transactions on Aerospace and Electronic Systems, **55**, 6 (2019), 3667-3673.

[33] Yardibi, T., Li, J., Stoica, P., Xue, M., and Baggeroer, A. B.
Source localization and sensing: a nonparametric iterative adaptive approach based on weighted least squares.
IEEE Transactions on Aerospace and Electronic Systems, **46**, 1 (2010), 425−443.

[34] Sun, H., Lu, Y., and Lesturgie, M.
Experimental investigation of iterative adaptive approach for ground moving target indication.
In *Proceedings of the IEEE International Conference on Radar (RADAR)*, **1** (2011), 715−718.

[35] Li, J., Zhu, X., Stoica, P., and Rangaswamy, M.
High resolution angle-doppler imaging for MTI radar.
IEEE Transactions on Aerospace and Electronic Systems, **46**, 3 (2010), 1544-1556.

[36] Zohdy, M. A., and Adamczyk, B.
Least squares approach to constrained global optimization.
In *Proceedings of the IEEE Conference on Decision and Control*, **1** (1991), 945−946.

[37] Rosen, P. A., and Davis, M. E.
A joint space-borne radar technology demonstration mission for NASA and the air force.
In *Proceedings of the IEEE Aerospace Conference*, 2003, 437−444.

[38] Xu, J., Liao, G., Zhu, S., and Zhang, X.
Clutter spatial-temporal characteristics for forward-looking missile-borne diving radar.
IEEE International Conference on Signal Processing, Communication and Computing, ICSPCC, 2012, 47−50.

[39] Wang, Z., and Liu, Z. P.
Aero-elastic stability design of spinning ballistic missile with sliding mode control.
International Conference On Computer Design and Applications, ICCDA, **3** (2010), 147−152.

[40] Wang, Z., Zhou, J., and Zhou, F.
The Aero-elastic characteristic of the low speed spinning ballistic missile and its stability design.
Measurement & Control Technology, **26**, 10 (2007).

[41] Choi, I., Park, S., Kim, S., Lee, S., and Kim, K.
Estimation of the micro-motion parameters of a missile warhead using a micro-Doppler profile.
IEEE Radar Conference (RadarConf), 2016, 1−5.

[42] Boutelle, J., Kau, S., and Marino, C.
ICBM reentry vehicle navigation system development at Honeywell.
IEEE Position Location and Navigation Symposium, 1998, 294−302.

[43] Pechier, M., Guillen, P., and Cayzac, R.

A combined theoretical-experimental investigation of Magnus effects.
16th AIAA Applied Aerodynamics Conference, 1998.

[44] Li, K., Yang, S., and Zhao, L.
Stability missiles with an Acceleration autopilot.
Journal of Guidance Control & Dynamics, **35**, 3 (2015), 774−786.

[45] Sun H., and Liu, Z.
Micro-doppler feature extraction for ballistic missile warhead.
IEEE International Conference on Information & Automation, 2008, 1333−1336.

[46] Liu, L., McLernon, D., Ghogho, M., and Hu, W.
Micro-Doppler extraction from ballistic missile radar returns using time-frequency analysis.
IEEE International Symposium on Wireless Communication Systems, 2010, 780−784.

[47] Zhao, Y., Shen, X., and Liang, J.
A novel micro-motion model for ballistic missile targets identification.
In *Proceedings of IEEE CIE International Conference on Radar*, 2011, 604−608.

[48] Sun, Z., Li, B., and Lu, Y.
Research on micro-motion and micro-Doppler of ballistic targets.
IET International Radar Conference, 2009, 1−4.

[49] Yan, X., Yang, S., and Zhang, C.
Analysis of stability for coning motion of rockets based on theory of nutation movement.
Acta Armamentarii, **30**, 10 (2009), 1291−1296.

[50] Kong, H., Jiang, H., Zhu, W., Zhang, X., and Zhu, C.
Research on a method of stability analysis for conical motion of rotating missile.
Flight Control & Detection, **3**, 1 (2020).

[51] Thomas, G. B.
Calculus and analytic geometry.
Mathematical Gazette. **44**, 2 (1961).

[52] Raney, J. R.
The theory and design of chirp radars.
Bell System Technical Journal, **39**, 4 (1960), 745−809.

[53] Borsari, G. K.
Mitigating effects on STAP processing caused by an inclined array.
Proceedings of the 1998 IEEE Radar Conference, 1998, 135-140.

[54] Himed, B., Zhang, Y., and Hajjari A.
STAP with angle-Doppler compensation for bistatic airborne radars.
Proceedings of the 2002 IEEE Radar Conference, 2002, 311-317.

[55] Varadarajan V. and Krolik J. L.
Joint space-time interpolation for distorted linear and bistatic array geometries.
IEEE Transactions on Signal Processing, **54**, 3 (2006), 848-860.

[56] Heng C., Lim, and Mulgrew B.
Filter banks based JDL with angle and separate Doppler compensation for airborne bistatic radar.
International Radar Symposium, 2005, 583-587.

[57] Fallah A. and Bakhshi H.
Extension of adaptive angle-Doppler compensation (AADC) in STAP to increase homogeneity of data in airborne bistatic radar.
6th International Symposium on Telecommunications (IST), 2012, 367-372.

[58] Zatman M.
Circular arry STAP.
IEEE Radar Conference, 1999, 108-113.

[59] Lim C. H., See C. M. S., and Mulgrew B.
Non-linear prediction of inverse covariance matrix for STAP.
IEEE International Conference on Acoustics, Speech and Signal Processing, 2007, 921-924.

[60] Morchin, W. C.
Airborne Early Warning Radar.
Artech House, 1990.

Penghui Huang (M’17) was born in Jiangxi, China. He received the B.S. and PH.D. degrees in electrical engineering from Xidian University, Xi’an, China, in 2012 and 2017, respectively.

He joined in the School of Electronic Information and Electrical Engineering, Shanghai Jiao Tong University, Shanghai, China, in 2017. He was an Assistant Professor from 2017 to 2021, and he is currently an Associate Professor and a Ph.D adviser. His research interests include space-borne early warning radar system design, space-time adaptive processing (STAP), multi-channel sea clutter modeling, simulation, space-time property analysis, and robust suppression, distributed space-borne wide-area surveillance radar signal processing with ground moving target indication (GMTI) as well as air moving target indication (AMTI), space-borne HRWS-SAR imaging, ISAR imaging, and weak target detection and tracking. He was the recipient of the Prize for Excellent Ph.D. degree dissertation of the Chinese Institute of Electronics education in 2017, and also the recipient of the Prize for Excellent Ph.D. degree dissertation of the Shaanxi Province in 2019.

Dr. Huang is a Reviewer of the IEEE Transactions on Geoscience and remote sensing, the IEEE Transactions on Aerospace and Electronic Systems, the IEEE Transactions on Signal Processing, the IEEE Journal of Selected Topics in Applied Earth Observations and Remote Sensing, the IEEE Sensor Journals, the IEEE Geoscience and Remote Sensing Letters, etc.

Hao Yang was born in Sichuan, China. He received his B.S. degree in electronic and information engineering from Wuhan University, Wuhan, China and is pursuing the M.S degree with the School of Electronic Information and Electrical Engineering, Shanghai Jiao Tong University, Shanghai, China.

His research interests include space-time adaptive processing (STAP), sea clutter suppression, and range-ambiguous clutter modeling and simulation.

Zihao Zou was born in Zhejiang, China. He is pursuing the Ph.D. degree with the School of Electronic Information and Electrical Engineering, Shanghai Jiao Tong University, Shanghai, China.

His research interests include space-time adaptive processing (STAP), sea clutter modeling and simulation, and maritime target detection.

Xiang-Gen Xia (M'97, S'00, F'09) received his B.S. degree in mathematics from Nanjing Normal University, Nanjing, China, and his M.S. degree in mathematics from Nankai University, Tianjin, China, and his Ph.D. degree in electrical engineering from the University of Southern California, Los Angeles, in 1983, 1986, and 1992, respectively.

He was a Senior/Research Staff Member at Hughes Research Laboratories, Malibu, California, during 1995-1996. In September 1996, he joined the Department of Electrical and Computer Engineering, University of Delaware, Newark, Delaware, where he is the Charles Black Evans Professor. His current research interests include space-time coding, MIMO and OFDM systems, digital signal processing, and SAR and ISAR imaging. Dr. Xia is the author of the book Modulated Coding for Intersymbol Interference Channels (New York, Marcel Dekker, 2000).

Dr. Xia received the National Science Foundation (NSF) Faculty Early Career Development (CAREER) Program Award in 1997, the Office of Naval Research (ONR) Young Investigator Award in 1998, and the Outstanding Overseas Young Investigator Award from the National Nature Science Foundation of China in 2001. He received the 2019 Information Theory Outstanding Overseas Chinese Scientist Award, The Information Theory Society of Chinese Institute of Electronics. Dr. Xia has served as an Associate Editor for numerous international journals including IEEE Transactions on Signal Processing, IEEE Transactions on Wireless Communications, IEEE Transactions on Mobile Computing, and IEEE Transactions on Vehicular Technology. Dr. Xia is Technical Program Chair of the Signal Processing Symp., Globecom 2007 in Washington D.C. and the General Co-Chair of ICASSP 2005 in Philadelphia.

Guisheng Liao (M’96~SM’16) was born in Guiling, China. He received the B.S. degree from Guangxi University, Guangxi, China, and the M.S. and Ph.D. degrees from Xidian University, Xi’an, China, in 1985, 1990, and 1992, respectively.

He is currently a Professor with Xidian University, where he is also Dean of School of Electronic Engineering. He has been a Senior Visiting Scholar in the Chinese University of Hong Kong, Hong Kong. His research interests include synthetic aperture radar (SAR), space–time adaptive processing, SAR ground moving target indication, and distributed small satellite SAR system design. Prof. Liao is a member of the National Outstanding Person and the Cheung Kong Scholars in China.